SANDIA REPORT

SAND2015-3571
Unlimited Release
Printed May, 2015

Evaluation of Computational Method of High Reynolds Number Slurry Flow for Caverns Backfilling

Giorgia, Bettin

Prepared by
Sandia National Laboratories
Albuquerque, New Mexico 87185 and Livermore, California 94550

Sandia National Laboratories is a multi-program laboratory managed and operated by Sandia Corporation, a wholly owned subsidiary of Lockheed Martin Corporation, for the U.S. Department of Energy's National Nuclear Security Administration under contract DE-AC04-94AL85000.

Issued by Sandia National Laboratories, operated for the United States Department of Energy by Sandia Corporation.

Available to DOE and DOE contractors from
U.S. Department of Energy
Office of Scientific and Technical Information
P.O. Box 62
Oak Ridge, TN 37831

Telephone: (865) 576-8401
Facsimile: (865) 576-5728
E-Mail: reports@adonis.osti.gov
Online ordering: http://www.osti.gov/bridge

Available to the public from
U.S. Department of Commerce
National Technical Information Service
5285 Port Royal Rd.
Springfield, VA 22161

Telephone: (800) 553-6847
Facsimile: (703) 605-6900
E-Mail: orders@ntis.fedworld.gov
Online order: http://www.ntis.gov/help/ordermethods.asp?loc=7-4-0#online

SAND2015-3571
Unlimited Release
Printed May, 2015

Evaluation of Computational Method of High Reynolds Number Slurry Flow for Caverns Backfilling

Giorgia Bettin
Geotechnology and Engineering Department
Sandia National Laboratories
P.O. Box 5800
Albuquerque, New Mexico 87185-MS0750

Abstract

The abandonment of salt caverns used for brining or product storage poses a significant environmental and economic risk. Risk mitigation can in part be addressed by the process of backfilling which can improve the cavern geomechanical stability and reduce the risk of fluid loss to the environment. This study evaluates a currently available computational tool, Barracuda, to simulate such processes as slurry flow at high Reynolds number with high particle loading. Using Barracuda software, a parametric sequence of simulations evaluated slurry flow at Reynolds number up to 15000 and loading up to 25%. Limitations come into the long time required to run these simulations due in particular to the mesh size requirement at the jet nozzle. This study has found that slurry-jet width and centerline velocities are functions of Reynolds number and volume fraction. The solid phase was found to spread less than the water-phase with a spreading rate smaller than 1, dependent on the volume fraction. Particle size distribution does seem to have a large influence on the jet flow development. This study constitutes a first step to understand the behavior of highly loaded slurries and their ultimate application to cavern backfilling.

Acknowledgments

The author wishes to thank Tim O'Hern for his help coordinating the laboratory experiments and Francis Hansen and Martin Nemer for technical review. The author also would like to credit Richard Jensen for the image processing and Jason Heath for the Post-processing data analysis.

TABLE OF CONTENTS

1 Scope of the Report 11

2 Background 13
2.1 Abandonment of Salt Caverns 13
2.2 Cavern Backfilling 14
2.3 Slurry Pipe Flow 15
2.4 Injection Flow of Slurry 16
2.4.1 Single Phase Jets 16
2.4.2 Slurry Jets 18
2.5 Computational Methods 19

3 Methodology 21
3.1 Experimental Apparatus 21
3.1.1 Slurry Jet Tank 21
3.1.2 Suspension 22
3.1.3 Image Analysis Procedure 23
3.2 Computational Analysis 24
3.2.1 Implementation Plan 24
3.2.1.1 Phase 1: Code Performance 24
3.2.1.2 Phase 2: Slurry Jet Analysis 26
3.2.2 Model Data Processing 28
3.2.2.1 Data management 28
3.2.2.2 Steady-state averaging 29
3.2.2.3 Jets size 29

4 Experimental results 31

5 Computational Results: phase 1 33
5.1 Preliminary Results 33
5.2 Mesh Sensitivity Analysis 34
5.3 Entrance Length Flow Development 35
5.3.1 Pipe flow 35
5.3.2 Small Tank 36
5.4 Flow velocity and Volume fraction dependence 38

6 Slurry Jets Results: Phase 2 41
6.1 Flow Rate Dependence 41
6.1.1 Fluid Velocity Distribution 41
6.1.2 Solid Velocity Distribution 43
6.1.3 Concentration Distributions 44
6.1.4 Jet Spreading 46
6.2 Volume Fraction Dependence 46
6.2.1 Fluid Velocity Distribution 47

6.3 Particle Size and Distribution Dependence 49
6.3.1 Particle Size Study 49
6.3.2 Particle Size Distribution 52
7 Conclusions 55
REFERENCES 56
Distribution 57

FIGURES

Figure 2-1: Current procedure for salt cavern abandonment. Prior to abandonment the product in the cavern is displaced with brine. All the entry wells are then cemented, isolating the 'bubble' of brine in the salt. 14
Figure 2-2: Schematic of a salt cavern that illustrates the three parts of solid backfilling process. a. Flow of slurry in pipes. b. Jet flow entrance into a cavern. c. Sedimentation of solid particles. 15
Figure 2-3: (left) Classification of different flow zones downstream of a single-phase free jet. (right) Schematic of the definition of jet half-radius width. 17
Figure 3-1: (top left) Table with length scale comparison between a model cavern and the tank used for our experiments (right) Image from the 2013 Sonar of West Hackberry site 117 cavern. (bottom left) Picture of experimental set up at SNL. 21
Figure 3-2: Particle size distribution of glass beads used in the experiments. 23
Figure 3-3: Progression of image processing. (a) Background image. (b) Unprocessed image showing the progression of the jet at an early time. (c) Jet image with subtracted background (d) Processed image showing multi-threshold gray scale. 23
Figure 3-4: Geometries used for Phase 1 of the study. (left) pipe, (center) small tank, (right) large tank. 24
Figure 3-5: Graphic representation of the simulations planned for phase one and the geometries used. 25
Figure 3-6: Graphic representation of the simulations run for phase 2. 28
Figure 3-7: Schematic of jet width calculation based on particles volume fraction. 30
Figure 4-1: (left) Image of slurry jet experiment as described in section 3.1. (right) Image of resultant mound at the end of the experiment. 31
Figure 4-2: Jet width as a function of distance from the jet inlet. For reference a plot of the single phase jet half size is shown. A is taken to be 0.1, while B = 0, as consistent with published values. 32
Figure 5-1: (Left) First simulation ran for the large tank geometry, Re 5000. Low resolution mesh does not capture the turbulent nature of the flow. (center) Same simulation but a medium resolution mesh, Re 5000. Small amount of instability seen in the shape of the jet. (right) High resolution simulation as it captures the jet vorticity. 33
Figure 5-2 Computational results for the small tank geometry for a low resolution (from the left), medium resolution and high resolution mesh. Simulations were run at Re 3200. The last two images on the right 'qualitatively' compare the results from the high resolution mesh simulation to the actual experiment. 34
Figure 5-3: Simulation results for dilute slurry (2%) in pipe geometry for a Re 5000. Figures were taken at simulation time of 12.4 sec. Computational particles are color coded by velocity magnitude. (Left) Close up of top of geometry where particles are introduced uniformly. (Right) Close up of bottom of geometry, flow exit. 35
Figure 5-4: Illustration of the geometries used to study the effect of entrance length into the small tank. 36
Figure 5-5: Comparison of the magnitude of downward velocity at the nozzle for the three simulations with varying entry length pipe. Figures are taken at the tank cross section. 37

Figure 5-6: Comparison of the jet shape for the three simulations with varying entry length pipe. Particles are shown to illustrate the onset of jet turbulence 38
Figure 5-7: Schematic of jet flow in small tank geometry for varying Re. 39
Figure 6-1: Fluid-phase downward velocity profile of simulation with Re 10000 as a function of radial distance for a series of depths. Depths are color coded by vertical distance, z/D. 42
Figure 6-2: Water phase centerline velocity (W_C) as a function of three different Re. The volume fraction for the simulations was kept constant at Φ=15 %. 42
Figure 6-3: Water phase jet width (b_w) as a function of depth (z/D) for three different Re flows. 43
Figure 6-4: Particle centerline velocity ($Velz_C$) as a function of three different Re. The volume fraction for the simulations was kept constant at Φ=15 %. 44
Figure 6-5: Volume fraction distribution profile of simulation with Re # 10000 as a function of radial distance for a series of depths. Depth are color coded by vertical distance, z/D. 45
Figure 6-6: Jet width based on particle concentrations as a function of depth for 3 different Re flows. 45
Figure 6-7: Jet spreading parameter λ , for different Re flows. 46
Figure 6-8: (top) Water phase centerline velocity (W_C) non-dimensionalized by W_{C0} (W_C at nozzle) for three different volume fractions. (bottom) Particle centerline velocity ($Velz_C$) non-dimensionalized by $Velz_{C0}$ ($Velz_C$ at jet nozzle) for different volume fractions. 47
Figure 6-9 Water phase jet width as a function of depth for different volume fraction slurries. 48
Figure 6-10: Jet spreading parameter λ , for varying volume fractions. 49
Figure 6-11: Illustration of jet shape as a function of particle size. 50
Figure 6-12: Water phase centerline velocity (W_C) non-dimensionalized by W_{C0} (W_C at nozzle) for different particle size slurries. 51
Figure 6-13: Water phase jet width as a function of depth for different particle size slurries. ... 51
Figure 6-14: Illustration of jet shape for a set of slurries with varying PSD. 52
Figure 6-15: Water phase centerline velocity (W_C) non-dimensionalized by W_{C0} (W_C at nozzle) for different particle size slurries. 53
Figure 6-16: Water phase jet width for different particle size slurries. 53

TABLES

Table 2-1: List of estimated values for geometry and slurry properties used to estimate flow regime for solid backfilling process. 16
Table 2-2: Effect of particle properties on slurry jets of various particle loading as found in the literature. (Φ is volume fraction, d is particle diameter)..... 19
Table 3-1: Values of slurry density and viscosity used for Re number calculation as a function of particles volume fraction. 22
Table 3-2: Phase 1 simulations parameters. LT =Large Tank, ST = Small Tank, PIP = Pipe..... 26
Table 3-3: Phase 2 simulations parameters..... 27
Table 5-1: Small tank set of simulations parameters and time requirement..... 38
Table 6-1: List of variable labels used for data processing. 41
Table 7-1 Effect of particle properties on slurry jets of various particle loading as found in the literature (in black) and as found in this study (in red). 55

NOMENCLATURE

DOE	Department of Energy
SNL	Sandia National Laboratories
SMRI	Solution Mining Research Institute
Re	Reynolds Number
CPFD	Computational Particle Fluid Dynamic
MP-PIC	Multiphase Particle-in-cells
PSD	Particle size distribution

1 SCOPE OF THE REPORT

In recent years, questions about the safety of current abandonment procedure for underground salt caverns have arisen. State regulators and industry operators are interested in safer methods for abandoning underground salt caverns. Rather than simply fill the void with brine, a safer method of solid backfilling has been proposed. This method offers the addition of a solid matrix with the potential to re-equilibrate in situ stresses; it additionally lessens the chance of hydrofracture through the drill string. Fundamental to this application is the placement of slurry into the cavern. The operation includes injection of fluid with exceptionally high solid fraction. This project aims to study slurry flow that has large solid volume fraction and a fast (high Re) flow. After evaluating the available computational tools we chose the Barracuda software to model this flow behavior. The features considered in this choice were the ability to fully couple the solid and fluid phase as well as the capability to simulate highly turbulent flow. The first part of this report focuses on the verification of the Barracuda software (a computational particles fluid dynamic method) as a viable tool to model high Reynolds number slurry flows. This report will evaluate how well the model can predict controlled flow behavior, as benchmarked by experimental data, as well as the solution algorithm stability, time and mesh size requirement.

The second part of this report will describe the results from the study of slurry jets and in particular the spreading of the jet and particles as a function of flow velocity, volume fraction and particle size.

2 BACKGROUND

2.1 Abandonment of Salt Caverns

The stability of underground salt caverns is a serious concern that has been brought to light by recent catastrophic failures resulting in the formation of sinkholes. The most recent being the sinkhole near the community of Bayou Corne, LA that appeared in August 2012.

Caverns are created in salt formations for storage of oil or gas, or for the purpose of salt mining. This practice is widespread worldwide and it has resulted in a vast number of caverns, many of which are now ageing and due to be abandoned. The long-term stability of abandoned caverns is of special concern for those older caverns with odd shapes (geomechanically unstable) or large depth. Additionally the possibility of using salt caverns for waste disposal has brought forward interest in their long term-behavior. A comprehensive compilation of the relevant research (close to 200 papers) up to 1997 was assembled by the Solution Mining Research Institute (SMRI) in a document titled 'Bibliography for Cavern Abandonment' [1]. The main concerns regarding abandoned caverns are the release of fluid to the environment and the mechanical failure of the cavern structure which can result in the formation of sinkholes. Current procedure for cavern abandonment consists of filling the cavern with brine and cementing the wells connected to the surface. This procedure leaves an isolated 'brine bubble' embedded in the salt (see Figure 2-1). Depending on the conditions in the cavern (brine thermal expansion, salt creep, leaching) pressure at the top of the abandonment cavern can create tensile stresses in excess of the salt tensile strength [2]. The introduced microfractures have the potential to propagate upward and lead to brine loss.

The other failure mechanism for caverns is collapse of walls or cavern roof, usually due a combination of excessive geological stresses with geomechanically unstable cavern geometries. Structural failure is the main cause of sudden formation of sinkholes.

Improper abandonment can lead to environmental damage, risk to nearby populations and clean-up and management-response costs. Some suggestions for risk mitigation procedures, mostly addressing brine thermal expansion, have been proposed [3-5] but no mitigation for cavern structural instability is currently available.

A procedure for backfilling a cavern can provide a load-bearing structure to support both the cavern roof as well as the side walls while additionally reduce the risk of salt fracture. However, not enough is known on the process of solid transport in cavern-like geometries and the behavior of slurry jets.

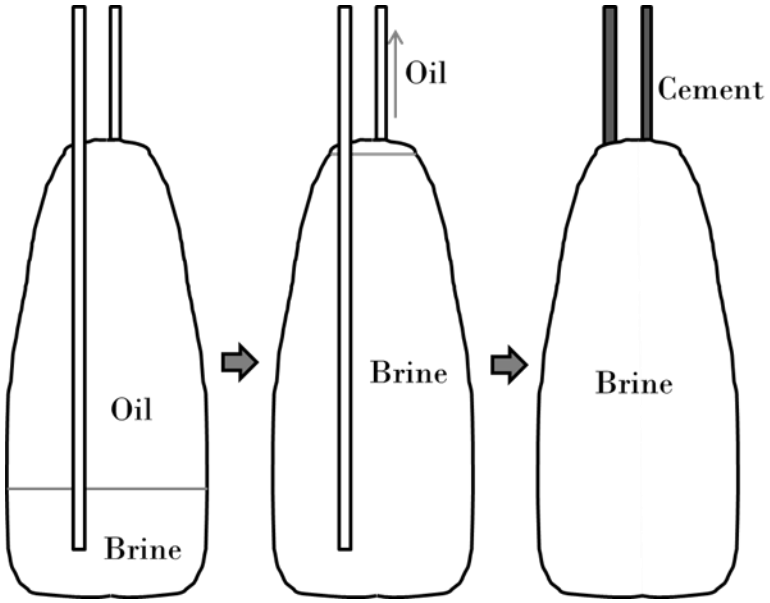

Figure 2-1: Current procedure for salt cavern abandonment. Prior to abandonment the product in the cavern is displaced with brine. All the entry wells are then cemented, isolating the 'bubble' of brine in the salt.

2.2 Cavern Backfilling

The backfilling of caverns with solid material presents a number of technological and logistical challenges. The complexity of the flow of solids (slurries), both down the well (pipe flow) and into the cavern, is dominated by the physical properties of the solids, such as size, shape, surface chemistry and as well as the flow parameters. As solids are introduced into the cavern, they fall out of suspension and brine is continuously removed until the solid accumulates and eventually forms a rigid matrix. The ultimate strength of the backfilling structure depends on how the solids distribute into the cavern and their sedimentation properties. Materials costs and availability, especially for caverns with large volumes, limit the type of solid materials and possibly their size and distribution that can be used for cavern fill. Considering the complexity of the process, it is useful to separate the problem in three parts: slurry flow in pipes, slurry injection jet in a 'semi-infinite' space, and the sedimentation of particles (see Figure 2-2). Although this study focuses on the injection of slurry jets, this approach will help us identify the dominant parameters for each phenomenon and help us gain some physical intuition on the backfilling process.

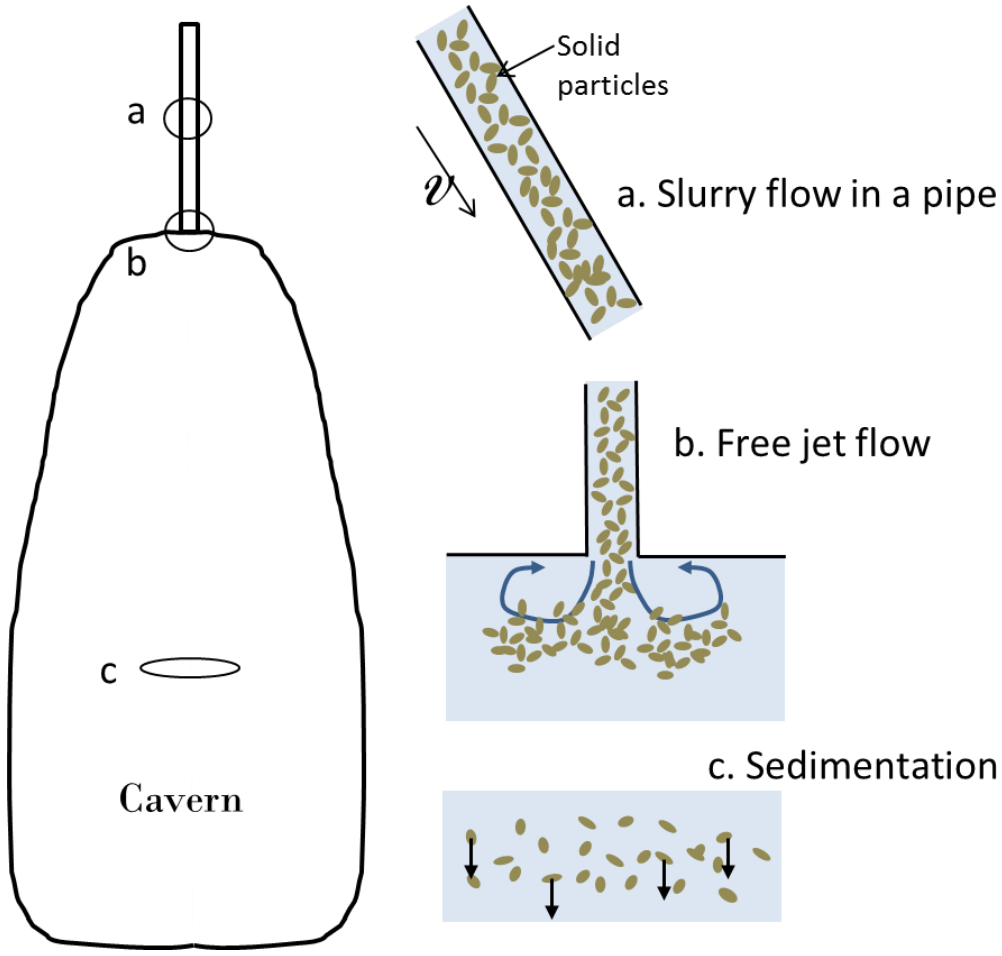

Figure 2-2: Schematic of a salt cavern that illustrates the three parts of solid backfilling process. a. Flow of slurry in pipes. b. Jet flow entrance into a cavern. c. Sedimentation of solid particles.

2.3 Slurry Pipe Flow

Flow of slurries and the transport of solid particles in pipes has been extensively studied. A detailed description of slurries and granular flow has been written by Brenner [6], but many other books and reviews are available in the open literature [7, 8]. Slurries made from smaller particles, less than a few μm in size, will generally behave like a uniform fluid and the solid phase will remain suspended. It is not the case for larger particles slurries, which can exhibit highly non-Newtonian behavior, and tend to separate from the suspending fluid. This creates a number of different phenomena ranging from accumulation of solids and pipe obstruction to a uniform distribution of particles in the pipe [8, 9]. In the case of salt caverns, the injection well is, in most cases vertical, which prevents the formation of dunes, beds and obstructions in general, but separation of particles mostly by size and density can still occur. From the backfilling point of view it is important to understand how solid separation and segregation in the pipe affect the jet development into the cavern because of its contribution to the spread of the solid particles.

The first step is to identify which flow regime will most likely exist during the backfill process. The flow Reynolds number (Re) based on the injection pipe diameter can be estimated by making a few simple assumptions based on the most likely geometry and the available resources for backfilling materials. Because of the large volume needed to fill a cavern we expect the solids to be most likely sand/silica or other byproducts from the mining industry (assumed density around 2600 kg/m^3) and to have a wide size distribution. This suggests that realistically, there will be a large portion of solids with dimensions greater than a few μm and therefore some degree of separation is expected; the amount of solids and size distribution will ultimately dictate the amount of separation and therefore the average viscosity of the slurry. For a first order estimate, we assume the solid volume fracture (Φ) to be around 15%, which still results in relatively low viscosities (estimated to be 10^{-2} Pa.s). For flow rates of 100 MBD (10^3 barrels per day)we estimated the Re based on the casing diameter to be around 10^5; Table 2-1 contains the numbers used for the estimation.

Pipe Diameter	D	30	[cm]
Viscosity	μ	10^{-2}	[Pa.s]
Density	ρ	1300	[Kg/m^3]
Velocity	V	2.5	[m/s]
Solid Volume fraction	Φ	15	[%]

Table 2-1: List of estimated values for geometry and slurry properties used to estimate flow regime for solid backfilling process.

2.4 Injection Flow of Slurry

The second part of the backfilling process is the entry of the slurry into the cavern. The injection zone and its geometry are extremely important because they govern the type of flow instability, the amount of mixing and the solid dispersion inside the cavern. For the purpose of backfilling, the goal is to disperse the particles away from the inlet (laterally) as much as possible and to reach a uniform mixing. These goals will help achieve a more uniform sedimentation. As seen in the previous section, the flow entering the cavern is highly turbulent. The study of slurry jets is relatively limited in the open literature and it has focus mainly on low Re numbers flows. As a starting point, it is still relevant to consider the behavior of a free jet (single phase) and the flow patterns it creates. The presence of solid particles will affect the physical mechanisms and the resultant phenomena. The impact will depend on the particles properties as well as their volume fraction. By understanding single phase behavior, we can assess the effect of the solid particles on the flow.

2.4.1 Single Phase Jets

Turbulent free jets, the characterization of flow around the nozzle, the specific velocity field and turbulence development have been widely researched both experimentally and computationally. One of the most important outcomes from these studies is the consensus that the inlet shape determines the downstream condition and the flow development (mixing) both in near and far fields. A very comprehensive review on the subject was published in 2012 by Ball

et. al [10], which highlighted the importance of inlet conditions and of course, the effect of Reynolds number. As we'll see in section 2.4.2 some of the conclusions from these studies are still relevant for slurry jets.

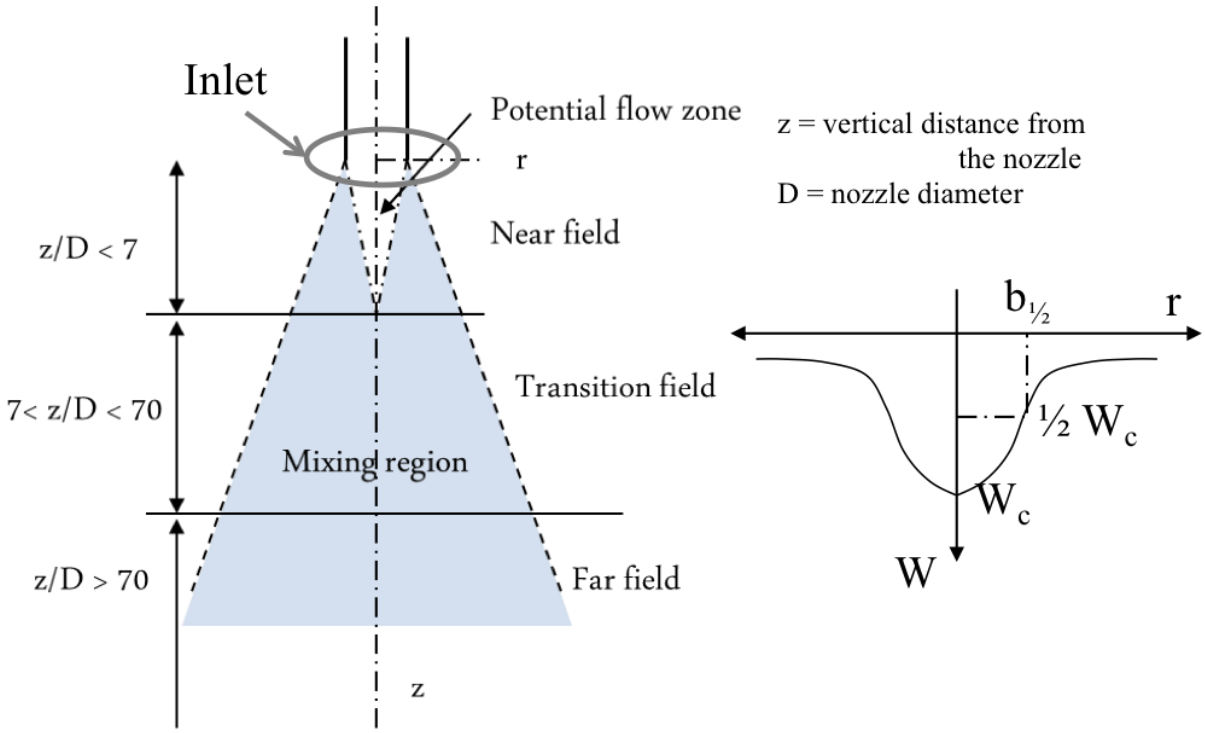

Figure 2-3: (left) Classification of different flow zones downstream of a single-phase free jet. (right) Schematic of the definition of jet half-radius width.

As a jet enters a semi-infinite space (in our case the cavern) and mixes with the surrounding fluid, turbulence is created. The flow field downstream of the inlet is composed of three regions; see Figure 2-3, which have different flow characteristics. The near field region is defined as the entrance zone. We note that along the z axis the area retains the characteristic of the pipe flow (defined as the 'potential' flow zone) while away from the centerline mixing starts to occur. By a distance z/D ≅ 7 the potential flow zone vanishes, and the flow enters the 'transition field zone'. The transition zone (usually 7<z/D<70 for a single phase fluid jet) is by definition where the whole region is turbulent and the greater part of mixing occurs. The region is particularly important because even small changes during this mixing/turbulence have great effect in the far field flow and velocity profiles. Once the flow reached a distance z/D>70 from the inlet it becomes uniform and the centerline velocity becomes proportional to the inverse of the distance from the inlet. This defines the beginning of the far field region. Ball et al. [10] described the decay of the centerline velocity as follows:

$$\frac{W_j}{W_c} = \frac{1}{B}\left(\frac{z}{D} - \frac{z_0}{D}\right) \qquad \textbf{(2-1)}$$

where W_j is the jet inlet velocity and W_c is the centerline velocity. The study summarized various values for B (decay constant) and z_0/D (virtual entrance) found in the literature to describe centerline velocity decays. Similarly the jet half-radius width was described as:

$$\frac{b_{1/2}}{D} = A\frac{z}{D} - B \qquad \text{(2-2)}$$

To note that this formulation is valid in the mixing zone only and therefore for z/D> 15.

2.4.2 Slurry Jets

The study of 2-phase jets, often referred as particle-laden or slurry jets is of importance for a variety of industrial and environmental application. These vary from waste-disposal, mining operation or hydro-transport as well as to enhance mixing and heat transfer in industrial processes. A number of studies have focused their effort in understanding the physics of slurry jets and how particle size and concentration affect turbulence development and spreading of the particles phase.

Difficulties in both experimental and computational tools [11] have limited studies of 2-phase jets to relatively low particle loading [12-14] (not more than a few percent) and a limited number of studies has focused on highly loaded jet behavior. Nonetheless some studies have been successful in experimental investigations of moderate solid concentrations. Parthasarathy and Faeth [15] were able to study the velocity and turbulence of glass-sphere slurry with volume loading up to 4.8%. And more recently Hall et al. [16] were able to study velocity and concentration profile as well as jet spreading for slurry with concentrations up to 12%.

Azimi et al. [17] conducted a computational study that was able to predict the behavior of slurry with volume fraction up to 8 %. For dilute or semi-dilute slurry it was found that the jet spreading rate depended on the volume fraction of the particles and that in fact, jet spreading was smaller for larger volume factions. The width of the jet was found to be similar to the single-phase jet closer to the jet injection, but became smaller at larger distances from the inlet. Additionally it was found that dilute solutions are sensitive to particle size, larger particles do reduce jet spreading. Large volume fraction slurries, on the other hand, are insensitive to particle size. One other parameter that was found to be affected by volume fraction is the jet centerline velocity. Hall et al.[16] and Azimi et al.[17] have shown that higher volume fraction resulted in an increase in centerline velocities. An attempt to summarized particles properties dependence on the jet characteristic as it was found in the literature is shown in Table 2-2.

Table 2-2: Effect of particle properties on slurry jets of various particle loading as found in the literature. (Φ is volume fraction, *d* is particle diameter).

		Jet spreading	Jet width	Centerline velocity
		λ	b_w	W_c
Single-phase	$\Phi = 0$		Linear increase with distance from the nozzle	Linear decay with distance from the nozzle
Dilute	$0 < \Phi < 1$	Decrease with Φ Decrease with larger *d*	Similar to single phase at small distances, but decrease farther from the nozzle	Same as single phase
Semi-dilute	$1 < \Phi < 5$	Decrease with Φ Insensitive to *d*	Similar to single phase at small distances, but decrease farther from the nozzle	Increase with Φ
Dense	$5 < \Phi < 15$			Increase with Φ
Very dense	$\Phi > 15$			

Radial distribution of both the water-phase velocity and concentration can be described as a Gaussian distribution and it has been found to be self-similar. Hall et al. [16] found that the centerline velocity of the particles reached a plateau and its magnitude was found to be greater than the particles terminal velocity. Also, the magnitude of the centerline velocity was found to increase with the slurry volume fraction. Azimi et al. [17] also noted that while larger particles have no impact on the centerline velocity decay, smaller particles results in an early velocity decay.

2.5 Computational Methods

Simulations of slurry flow are, in general, very complex and computationally expensive problems [11]. After evaluating different methods and commercially available computational packages we decided that the multiphase particle-in-cell (MP-PIC) method available by CPFD (Barracuda) was the most appropriate for the study of highly loaded slurry flows. This method maps the fluid into a Eulerian frame, where the volume is meshed to relatively large cells. A single value of fluid pressure and velocity is linked to each cell. Particles on the other hand, follow a Lagrangian frame and are allowed to enter/exit each cell while their trajectory is tracked [18]. This combination method allows us to reduce the computational effort to a reasonable time and still simulate large volumes of particles. Some of the advantages of this method are that it allows complete solution from dilute to close-packed particles loading contrary to most other methods where loading up to only 5-7 % is allowed. Additionally, it can handle particles of different sizes and density, as in polydisperse and multiple species solids. More details about this computational method are described by Snider et al. [18, 19].

This page intentionally left blank

3 METHODOLOGY

3.1 Experimental Apparatus

3.1.1 Slurry Jet Tank

An experimental apparatus was built at Sandia National Laboratory (SNL) to run a series of slurry jet experiments. The goal of these experiments was to gather jet dimension data to use as a benchmark to validate against the computational results. Image processing analysis was used to capture the jet shape and the turbulence development. The geometry was chosen to be representative of an underground salt cavern with similar diameter to jet inlet size ratio. The table in Figure 3-1 (top left) lists the various length scales taken into consideration when building the scaled down experiment. For simplicity the shape of an idealized cavern was taken to be a long cylinder, even though salt caverns can be of many different shapes. The ratio between the pipe diameter and the cavern/tank diameter was kept the same. The tank height was kept much shorter due to infrastructure constrains. A picture of the tank used in the experiments as well as a sonar image of a typical cavern is shown in Figure 3-1. The 30 gallons tank is hexagonal in shape, to minimize image distortion, and an approximate height of 2 ft.

	Cavern		Tank	
d	1	[ft]	1.25	[mm]
D	200	[ft]	0.5	[m]
L	2000	[ft]	0.6	[m]
d/D	5×10^{-3}		2.5×10^{-3}	
D/L	0.1		0.8	
d/L	5×10^{-4}		2.1×10^{-3}	

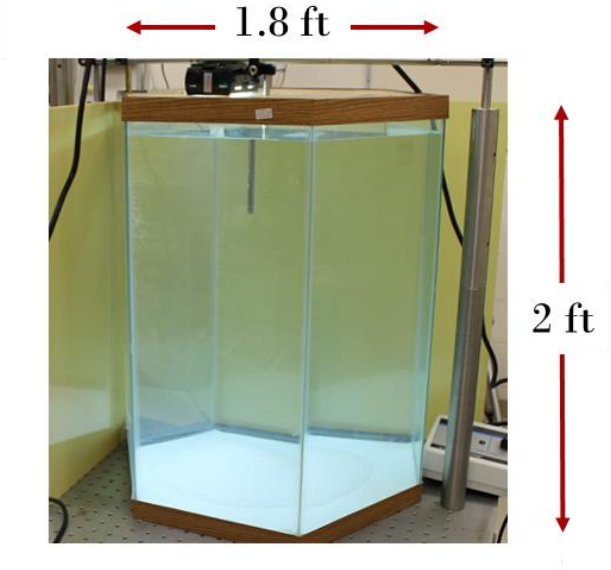

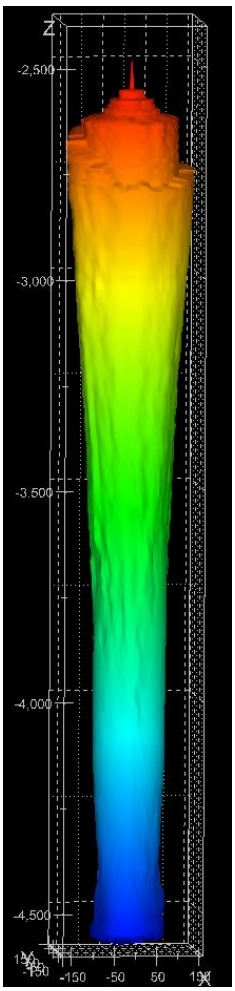

Figure 3-1: (top left) Table with length scale comparison between a model cavern and the tank used for our experiments (right) Image from the 2013 Sonar of West Hackberry site 117 cavern. (bottom left) Picture of experimental set up at SNL.

Flow was injected through the top of the tank with a small diameter pipe and it was characterized by estimating the Reynolds number as follows:

$$\boldsymbol{Re} = \frac{\boldsymbol{\rho DV}}{\boldsymbol{\mu}} \qquad \textbf{(3-1)}$$

where V is the average flow velocity across the pipe, D is the pipe diameter and ρ is the slurry density calculated from the slurry volume fraction Φ, as follow:

$$\boldsymbol{\rho_{slurry}} = \boldsymbol{\rho_{part.}} \cdot \phi + \boldsymbol{\rho_{fluid}}(\mathbf{1} - \phi) \qquad \textbf{(3-2)}$$

The slurry comprised spherical particles with a narrow size distribution and the values of the viscosity μ, as a function of volume faction, were taken from Metzger [20]. Table 3-1 contains the viscosity values used for the Reynolds number calculations.

Table 3-1: Values of slurry density and viscosity used for Re number calculation as a function of particles volume fraction.

Φ	[%]	0	2	10	15	25	35
ρ_{slurry}	[kg/m^3]	1000	1030	1153	1228	1380	1532
μ_{slurry}	[Pa.s]	0.001	0.001	0.0012	0.0019	0.0025	0.004

3.1.2 Suspension

The particles used in this experiment were glass beads with an initial nominal diameter that varied from 90-150 μm. The particles were suspended and decanted off to reduce the number of small particles. The distributions of the resultant particles was analyzed and the results shown in Figure 3-2. The volume fraction of the suspension was set to be 15%. A mixing tank was set up where the particles were continuously agitated by a set of rotating blades to prevent sedimentation. The resultant slurry was then pumped through the tubing into the experiment tank.

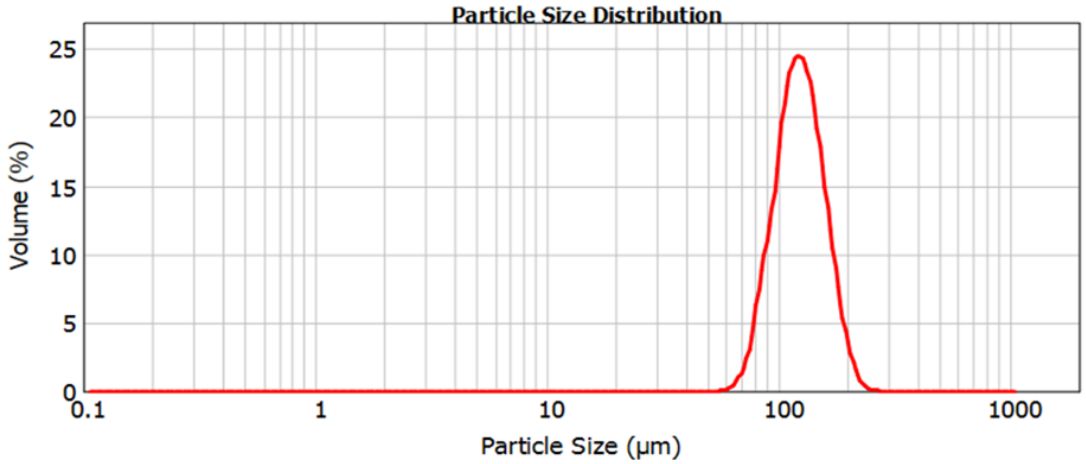

Figure 3-2: Particle size distribution of glass beads used in the experiments.

3.1.3 Image Analysis Procedure

The tank experiment movie was processed by using the ffmpeg code, an open-source utility[1], and individual images were extracted from the *.wmv video. All frames were extracted into individual jpeg images using the code, GraphicsConverter, version 8.8.3[2]. The images were cropped, enhanced and contrast increased. In order to study the shape of the jet, the background was subtracted. The images were then processed with multi-thresholding, to obtain a grayscale contours. This process is illustrated in Figure 3-3. To determine the size of the jet, the image was scanned, row by row, and based on the color of the pixels the size of the jet was determined.

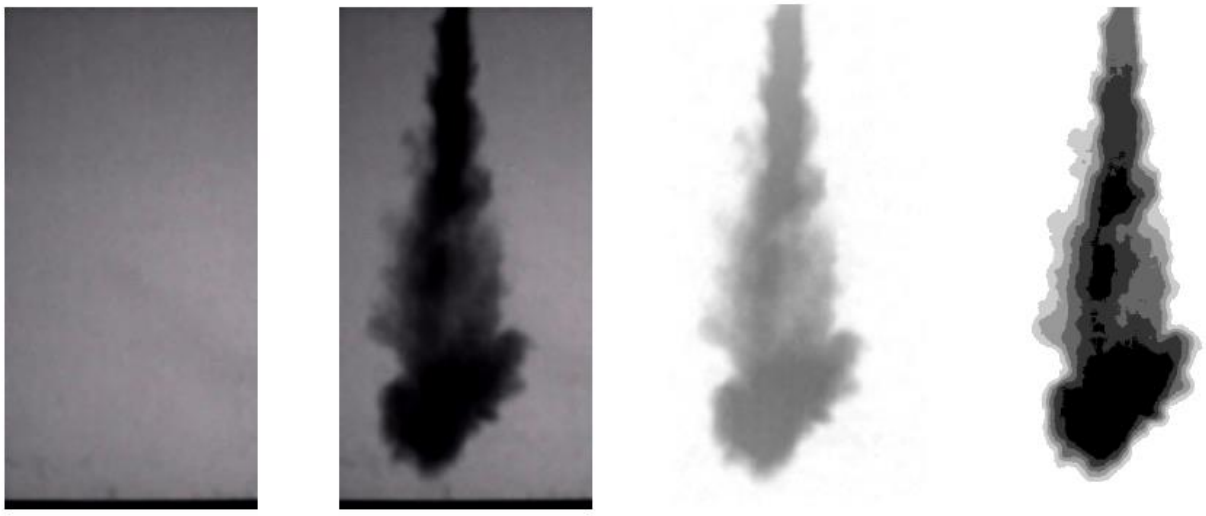

(a) (b) (c) (d)

Figure 3-3: Progression of image processing. (a) Background image. (b) Unprocessed image showing the progression of the jet at an early time. (c) Jet image with subtracted background (d) Processed image showing multi-threshold gray scale.

[1] ffmpeg.org

[2] GraphicsConverter is created by Lemke Software, LLC, www.lemkesoft.com

3.2 Computational Analysis

3.2.1 Implementation Plan

A plan was put into place to verify the code performance for the specific problem and define the framework for the analysis of the results. The plan included verification of the accuracy of the code (Barracuda) for simulations of highly loaded slurries in a suspending liquid. This differs from previous use to simulate particles flow in gases. A key point to verify is the ability to handle slurry flows at high Re in the turbulence regime. The plan also includes the study of the injection of slurry jets and how to scale the results up for applications in flow in large cavities and caverns.

3.2.1.1 Phase 1: Code Performance

The first phase of this plan is dedicated to the analysis of the predictive model as it applies to our system of highly loaded slurry at high Re number flows. In Phase 1 we utilize 3 different geometries: a pipe, a small tank and a large tank as shown in Figure 3-4. Each geometry is used to complete a specific task (question) and was chosen to minimize the simulation time and expedite the study. A graphical illustration of the organization of tanks in phase 1 is shown in Figure 3-5.

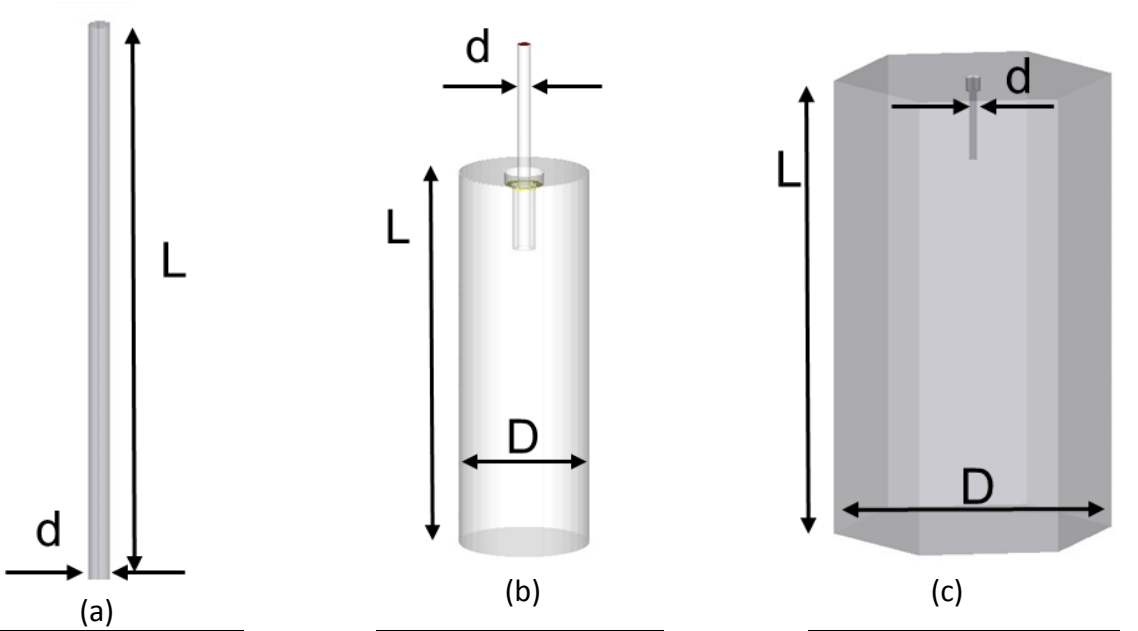

(a)

L	0.3	[m]
d	5×10^{-3}	[m]

(b)

L	0.25	[m]
d	5×10^{-3}	[m]
D	5×10^{-2}	[m]

(c)

L	0.8	[m]
d	7.5×10^{-3}	[m]
D	0.5	[m]

Figure 3-4: Geometries used for Phase 1 of the study. (left) pipe, (center) small tank, (right) large tank.

The pipe geometry was used to study the flow of slurry before the jet is created and specifically the development of in-pipe turbulence and time-average velocity profile. The focus of the pipe flow simulation was to verify the velocity profile in the inlet (before the jet is created) was accurately captured and define the minimal pipe length requirement for fully developed flow in this geometry. The same could have been accomplished by using the large tank geometry, but this smaller geometry allows for a reduction in the time for running each simulation.

The small tank was used to study the details of the turbulence and to conduct a study of the mesh sensitivity for this specific problem. As for the case of the pipe, the reduction in size of the geometry is due to the time needed for the simulation of the large tank. The size of the cells is limited by the length scale relevant for the turbulent flow as it exits the inlet. Restricting the tank in the radial direction allow us to still capture the turbulence development without carrying over the large spaces that, at small times, don't greatly influence the jet. The large tank is a one-to-one copy of the experimental set up used for benchmarking our results. The details and settings used for these simulations are based on the results from the pipe and small tank geometry. A table that includes the simulations conducted for phase 1 is shown in Table 3-2 and includes each simulation relevant parameters.

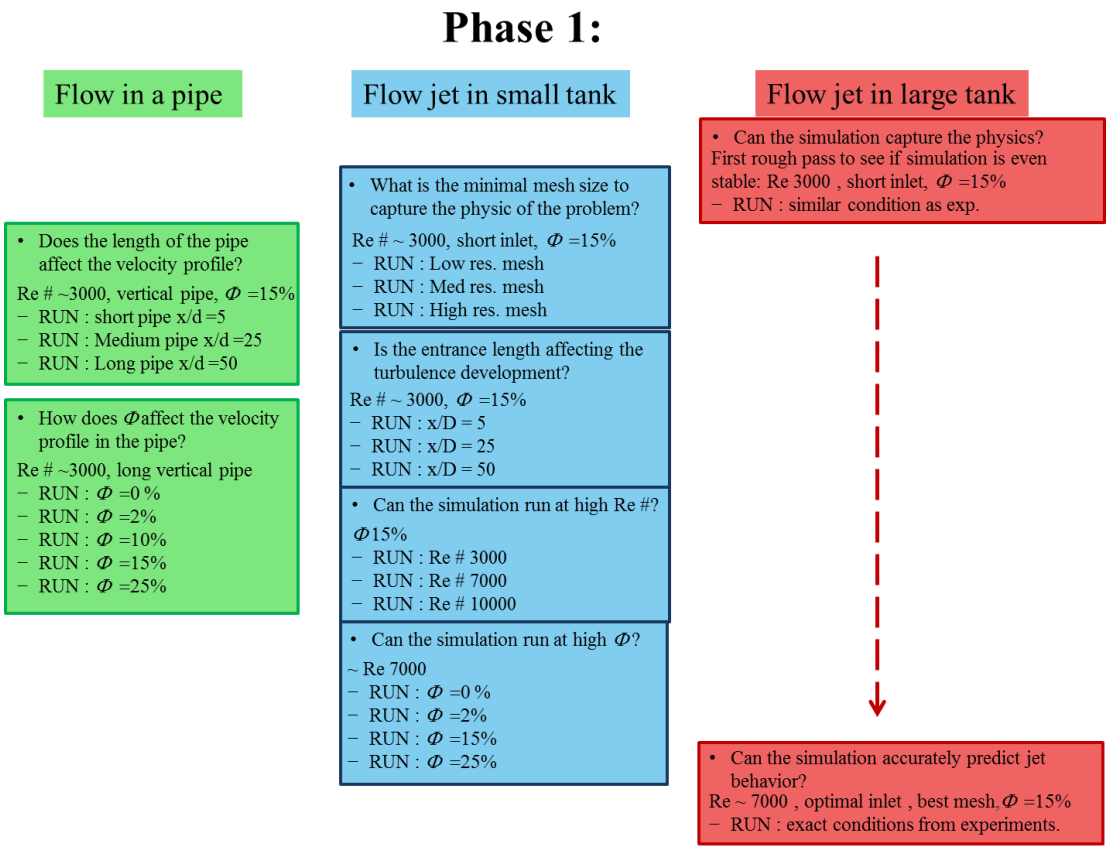

Figure 3-5: Graphic representation of the simulations planned for phase one and the geometries used.

Table 3-2: Phase 1 simulations parameters. LT =Large Tank, ST = Small Tank, PIP = Pipe

Simulation Code	ϕ	Re	Mesh	L/D	Particle Density [kg/m^3]
LT 2	15	4600	Med	5	2200
LT 3	13.6	4000	High	5	2520
LT 4	15.5	6000	High	5	2200
LT 5	15	7000	High	25	2520
ST 1	0	14000	High	25	2200
ST 2	2	14000	High	25	2200
ST 3	15	3000	High	25	2200
ST 4	15	7000	High	25	2200
ST 5	15	10000	High	25	2200
ST 6	25	7000	High	25	2200
ST 7	15	3200	Low	5	2200
ST 8	15	3200	Med	5	2200
ST 9	15	3200	High	5	2200
ST 11	15	3200	High	50	2200
PIP 1	0	5000	High	50	2520
PIP 2	2	5000	High	25	2520
PIP 3	2	5000	High	50	2520
PIP 4	10	5500	High	50	2520
PIP 5	15	5500	High	50	2520
PIP 6	25	5500	High	50	2520

3.2.1.2 Phase 2: Slurry Jet Analysis

Phase 2 is concerned with the physics of slurry jets and the development of turbulence as the jet enters the tank. In particular we're interested in the effect of the following on the jet development:

- Flow velocity (Re)
- Particle loading (Φ)
- Particle size and distribution (PSD)

A separate study is currently looking at the possible pumping rates and particle properties as they would be available for cavern abandonment backfilling. This will allow us to limit the parameter space to the relevant ones. A graphical illustration of the organization of tanks in phase 2 of this project is shown Figure 3-6 while the details of the simulations parameters are included in Table 3-3.

Table 3-3: Phase 2 simulations parameters.

Simulation Code	ϕ	Re	Particle size [μm]	L/D
LT 6	15	3000	90-150	25
LT 5	15	7000	90-150	25
LT 7	15	10000	90-150	25
LT 8	1	10000	90-150	25
LT 9	5	10000	90-150	25
LT 7	15	10000	90-150	25
LT 10	25	10000	90-150	25
LT 11	15	10000	5	25
LT 12	15	10000	15	25
LT 13	15	10000	150	25
LT 14	15	10000	1-5	25
LT 15	15	10000	50-100	25
LT 16	15	10000	5-100	25

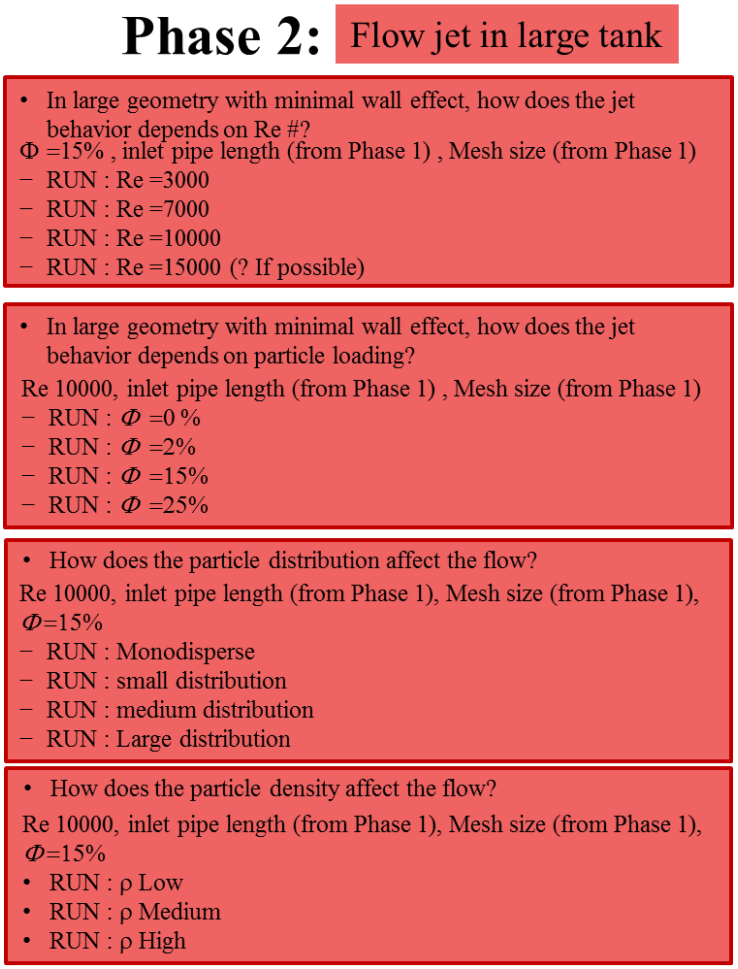

Figure 3-6: Graphic representation of the simulations run for phase 2.

3.2.2 Model Data Processing

3.2.2.1 Data management

Post-processing of Barracuda simulation output included major steps of: conversion of binary output to text files; paring of text files; import of text files into Matlab; and a variety of data organization, processing, and analysis activities using Matlab scripts specifically written for this project. Conversion of binary output and paring involved Python scripts obtained from Computation Particle Fluid Dynamics, LLC, the developers of Barracuda software. Paring involved selection of only key data columns required for subsequent analysis and plotting. Paring was required to reduce data processing time as the text file output of the 11 separate simulation cases totaled approximately four Terabytes. Import and organization with Matlab involved placement of data into Matlab structure arrays, one for each simulation output time. Organization of data associated with the grid cells of the simulations involved extraction of layers of data output at given z depths. Particle data for the same given z depths required extraction of data for bins or z-depth intervals centered on the same z-depths selected for the cell data post processing. Thus, Matlab was used to create ".mat" files of organized output data for given output times and z depth intervals, which were then subsequently and sequentially

loaded into Matlab for further post processing. Sequential loading of the ".mat" files was necessary as the files were themselves large—loading all data at once exceeded the 16 GB Ram of the workstation used for post processing and would crash Matlab.

3.2.2.2 Steady-state averaging

Scripts were written to determine vertical fluid velocity at the centroid of the simulated tank in the xy-plane for the given z-depths. Iteration showed that at least 50 z-depths for plotting, from the slurry injection nozzle to the base of the tank, were required to minimize data-extraction-based artifacts (e.g., jags) in the plots of the data. The centerline fluid velocity was examined to determine steady-state by plotting output time of centerline velocity versus depth for 10 equal time intervals that spanned the total output time. The time intervals were cumulative, meaning that the first included all output times, the second started a later time and included all output from that time onward, and so on. Visual inspection allowed for selection of a "steady-state" time when early-time non-physical transients had passed and the data exhibited similar behavior and variance. For a given z-depth, data were averaged from the steady-state time using output at that time and all later output. The simulations did not appear to exhibit any "late-time" behavior, or behavior at later times that was much different from the steady-state behavior. The vertical fluid centerline velocity-based steady-state time was used as steady-state time for all other types of data averaging and plotting, including fluid and particle jet widths, the particle centerline velocity, and vertical fluid distributions in the xy-plane. Particle centerline velocity calculations required binning and arithmetic averaging of data within rectangular regions centered on the given z-depths and the four cells boundaries centered on the center of the tank in the xy plane. Arithmetic averaging of radially-binned vertical fluid velocity in the xy-plane was performed. Trial and error indicated that logarithmic binning does not properly capture and reflect that gridding of the underlying mesh and the trends in the data. Binning based on the "compound interest" formula was employed, which better captured and displayed the data for the given grids using a reasonable number of bins (approximately 205).

3.2.2.3 Jets size

Jet spreading widths included those for fluid and particle data using the aforementioned steady-state averaged data. The fluid spreading width at 50% of the centerline velocity was calculated by first calculating 50% of the centerline velocity and then searching for a value within ±10% of that value in the radially-averaged data of the xy plane. Similar particle centerline velocities were calculated for particle volume fractions of 50%, 20%, and 10% of the particle centerline velocity, see Figure 3-7.

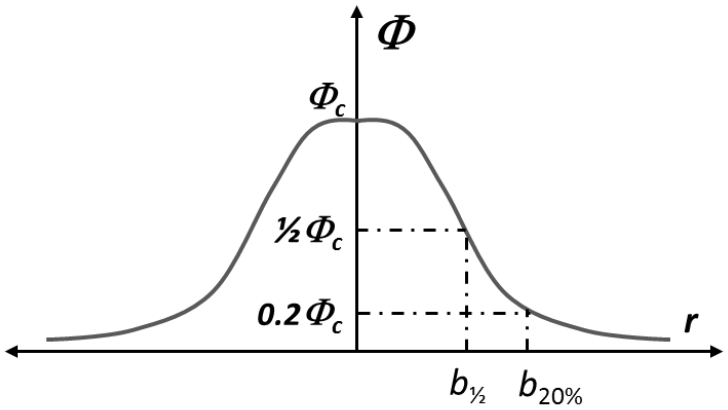

Figure 3-7: Schematic of jet width calculation based on particles volume fraction.

4 EXPERIMENTAL RESULTS

As described in section 3.1.3., images from the tank experiment were processed and analyzed. A sample image of the jet shape is shown in Figure 4-1 as well as one that illustrates the shape of the mound after the experiment was finished.

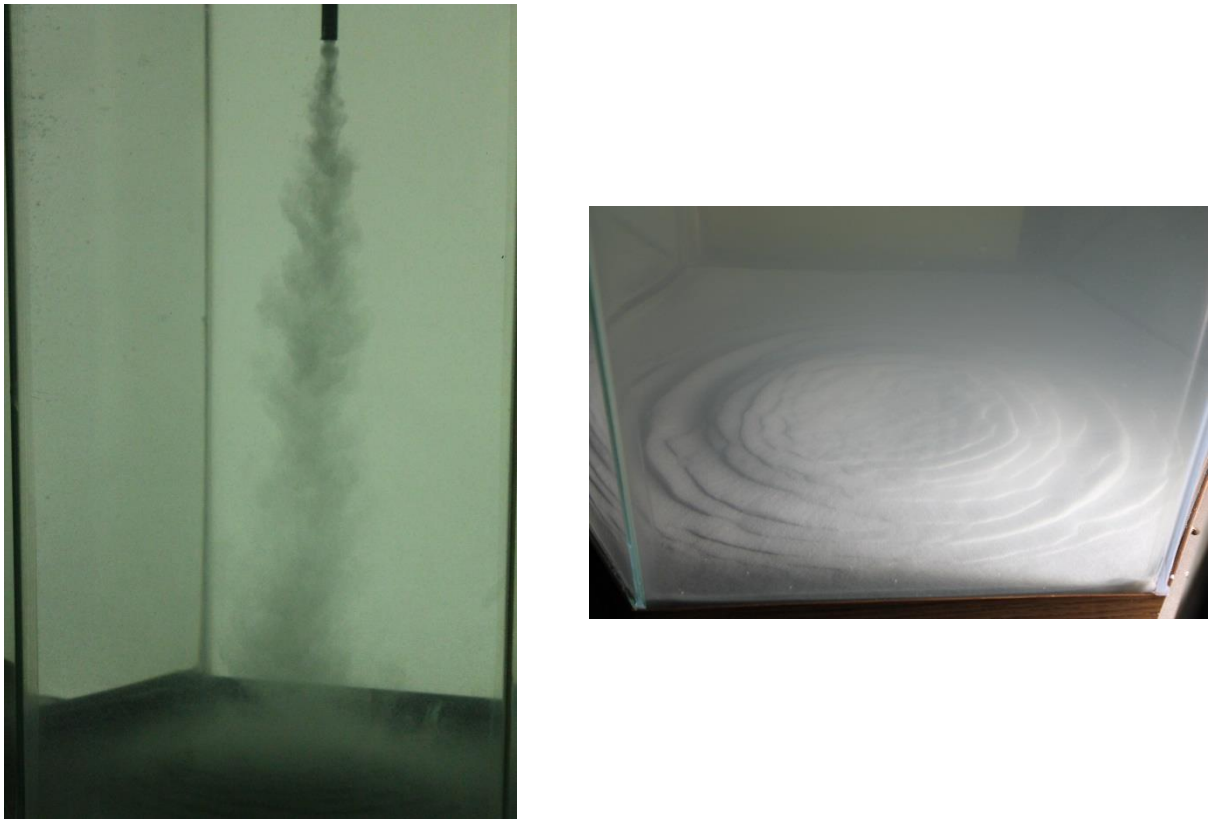

Figure 4-1: (left) Image of slurry jet experiment as described in section 3.1. (right) Image of resultant mound at the end of the experiment.

The results from the analysis of the jet size are presented in Figure 4-2 and show a linear relation between the size of the jet and the distance to the jet inlet. To note that in our analysis we take the size as the most outer point where particles are seen. The rate of jet spreading is found to be consistent with equation (2-2) presented in Ball et al. [10], and the relation is plotted, for reference in the same figure. For the ideal single phase jet, A was taken to be 0.1 and B=0. A linear fit to our experimental data found a spreading rate, slope A= 0.11. The offset of the experimental results as compared to the single phase jet model is due, at least in part, to the fact that b_w is by definition the jet half size, while the experimental result was taken at the maximum jet width.

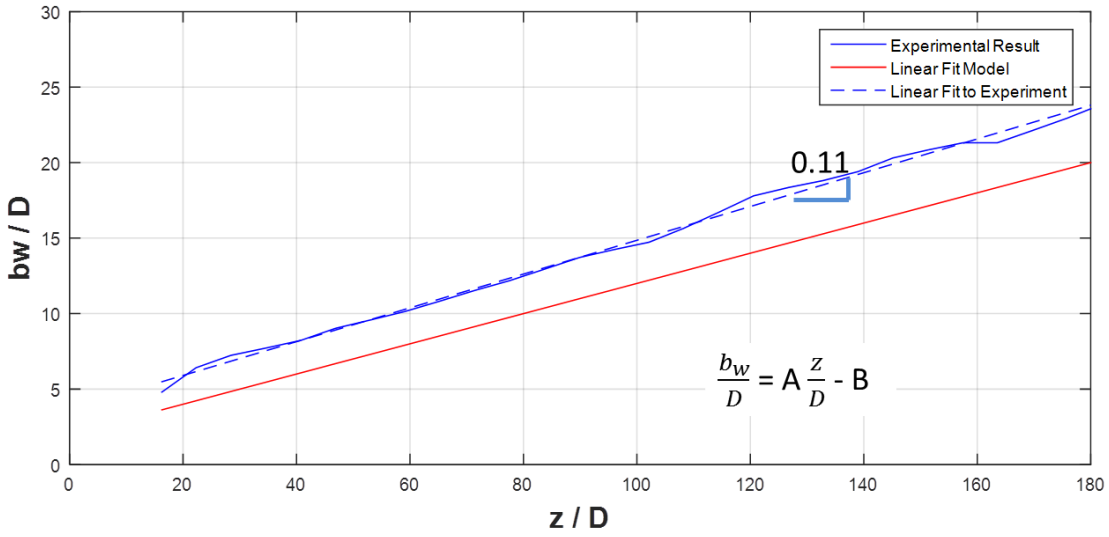

Figure 4-2: Jet width as a function of distance from the jet inlet. For reference a plot of the single phase jet half size is shown. A is taken to be 0.1, while B = 0, as consistent with published values.

5 COMPUTATIONAL RESULTS: PHASE 1

5.1 Preliminary Results

An initial simulation was run to understand the stability of the code at the desired Re and volume fraction of particles (Φ). The simulation was run at Re of 5000 and a relatively low number of cells (350k). The mesh was sized to account for 5 cells across the orifice and the cells increased in size in the radial direction. The simulation proved to be stable but no turbulence was produced, inconsistent with experimental results. We suspected this to be due to the relatively large size of the computational cells. The same simulation was run with 9 cells across the orifice (yielding 1.2M cells). Despite taking longer to run, this showed a small amount of turbulence development suggesting, in fact that in order to capture the vorticity of the turbulence, smaller cells were needed. A more detailed description of the mesh sensitivity analysis will be described in section 5.2. A final simulation that utilized a high resolution mesh was run and confirmed that in fact small cells size are necessary to fully capture the physics of the problem; a visual comparison between the 3 simulations is shown in Figure 5-1.

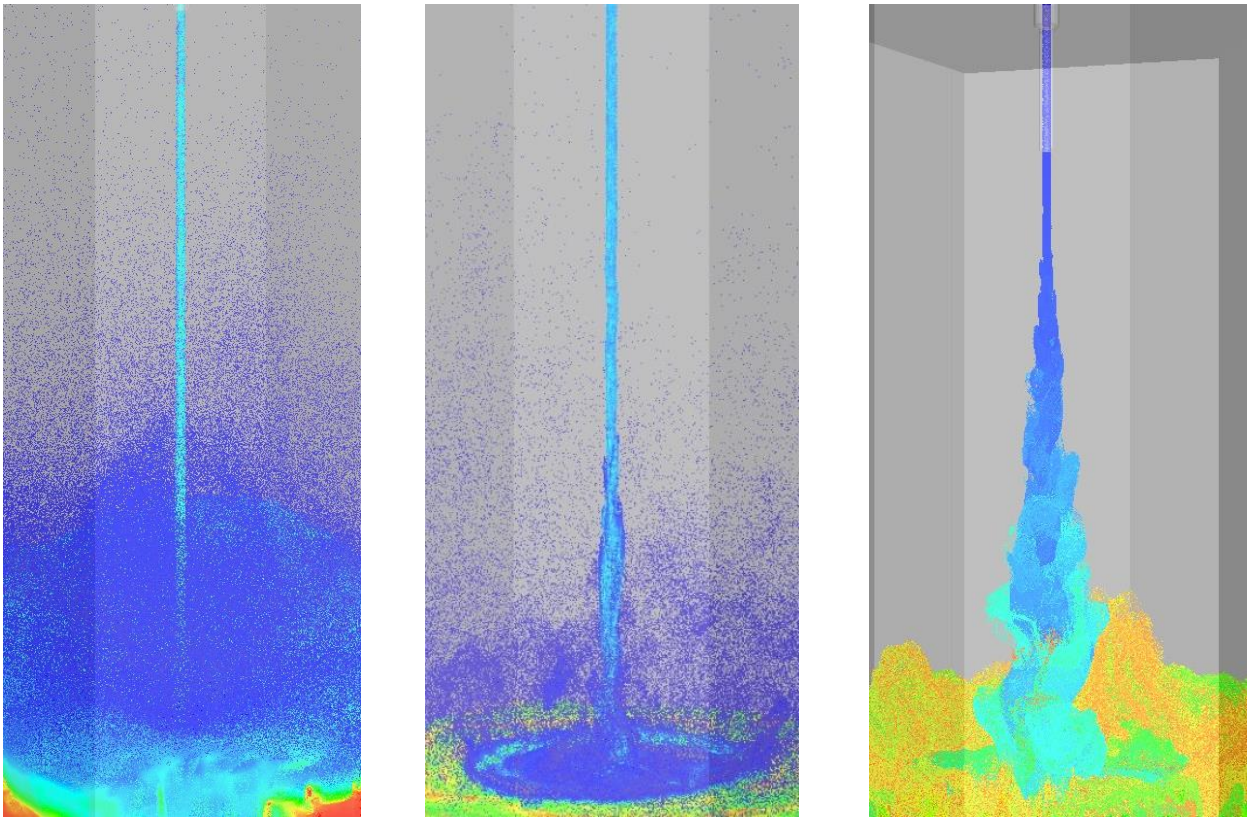

Figure 5-1: (Left) First simulation ran for the large tank geometry, Re 5000. Low resolution mesh does not capture the turbulent nature of the flow. (center) Same simulation but a medium resolution mesh, Re 5000. Small amount of instability seen in the shape of the jet. (right) High resolution simulation as it captures the jet vorticity.

5.2 Mesh Sensitivity Analysis

The first most important issue, as we started to evaluate the code, was the size requirement for the mesh. To capture the turbulence of the jet, cells size needed to be at least as small as the relevant turbulence length scale. On the other hand, a large number of cells not only take a tremendous amount of time to calculate, but also uses a lot of computer power. To find the optimal cell size for physical fidelity, the small tank geometry was used to run three simulations with decreasing cells size. The size of the cells was scaled with the diameter of the pipe and the low resolution was defined as 5 cells across the diameter yielding a mesh with 380k cells. The medium resolution was set to have 9 cells across the diameter (600k) while the high resolution had 15 cells across (1.4 M cells). The size of the cells was increasing smoothly in the radial direction. Figure 5-2 shows the flow of particles after 1 simulated second for all three mesh sizes. As can be seen from the first image on the left, the low resolution mesh doesn't capture the development of the jet, and very little turbulence, is seen. This is consistent with the results from our first rough simulation (section 5.1). As we increased the mesh resolution we notice that the simulation is starting to show some turbulence along the jet, even if not quite enough to match with the experimental results. The results from this series of simulation found that, in order to capture the physics of the jet, a high resolution mesh, with at least 15 cells across the pipe diameter is necessary. The two right pictures on Figure 5-2 show a comparison between the simulated and experimental results. One thing to stress is that the accuracy of the results are not just based on the mesh size inside the pipe, but the cells around the orifice needs to stay small for a few diameter away in the radial direction.

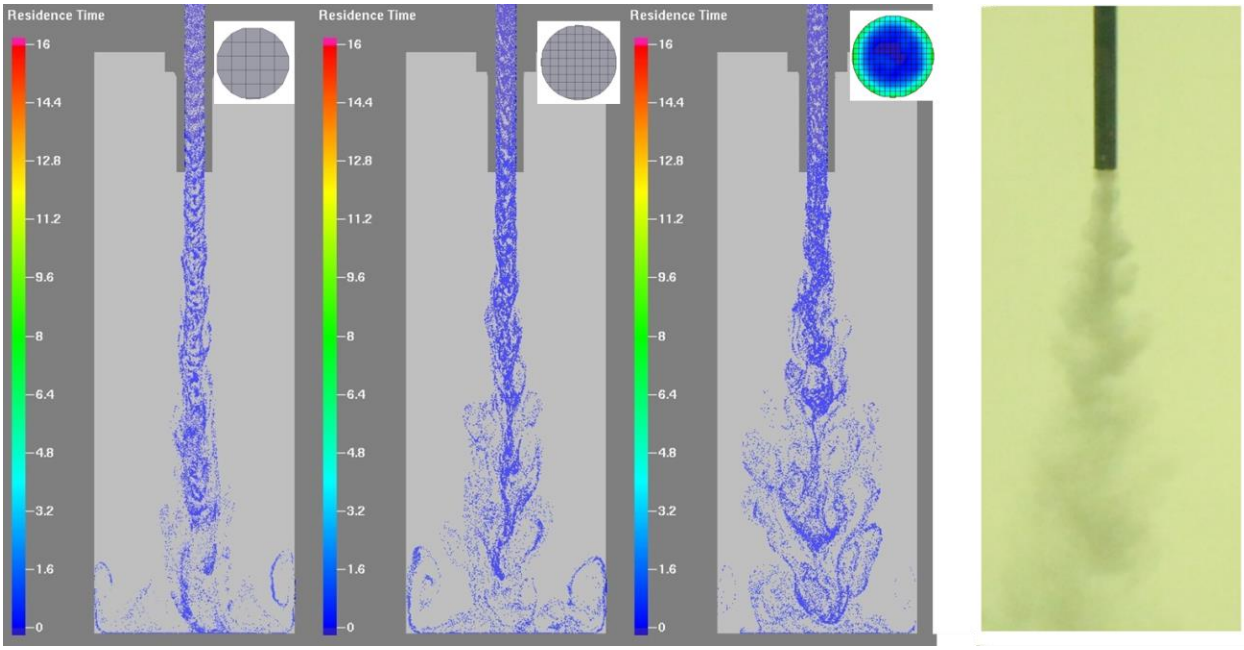

Figure 5-2 Computational results for the small tank geometry for a low resolution (from the left), medium resolution and high resolution mesh. Simulations were run at Re 3200. The last two images on the right 'qualitatively' compare the results from the high resolution mesh simulation to the actual experiment.

A similar study was conducted for the large tank geometry. Due to the long time requirement only a few seconds were simulated, but it was enough to verify that in fact a high resolution mesh was necessary to capture the physics of the problem. Also a delayed appearance of turbulence close to the orifice was found. This is suspected to be due to the nature of the flow in the pipe and therefore a study of pipe flow was initiated.

5.3 Entrance Length Flow Development

5.3.1 Pipe flow

The study of slurry flow in pipe geometry was necessary to understand how the velocity profile develops as a function of pipe length and flow regime. In particular, it was found that if the pipe flow had not transitioned to fully turbulent before the nozzle, the jet development in the simulation was delayed.

A series of simulations that utilized the pipe geometry were run as a function of pipe length and particle volume fraction. In the simulations the slurry was introduced at the top of the pipe with uniform velocity (both water phase and particles) and with uniform particle distribution. This is illustrated in Figure 5-3 (left). As the slurry travels downward though the pipe a parabolic velocity profile is developed in both phases approaching zero velocity at the walls. Figure 5-3 (right) illustrates the particles velocity and spatial distribution at the pipe exit for a dilute solution (2%). To note that as a result of slower velocity along the wall, particles tend to accumulate along the wall with a minimum concentration at the center of the pipe.

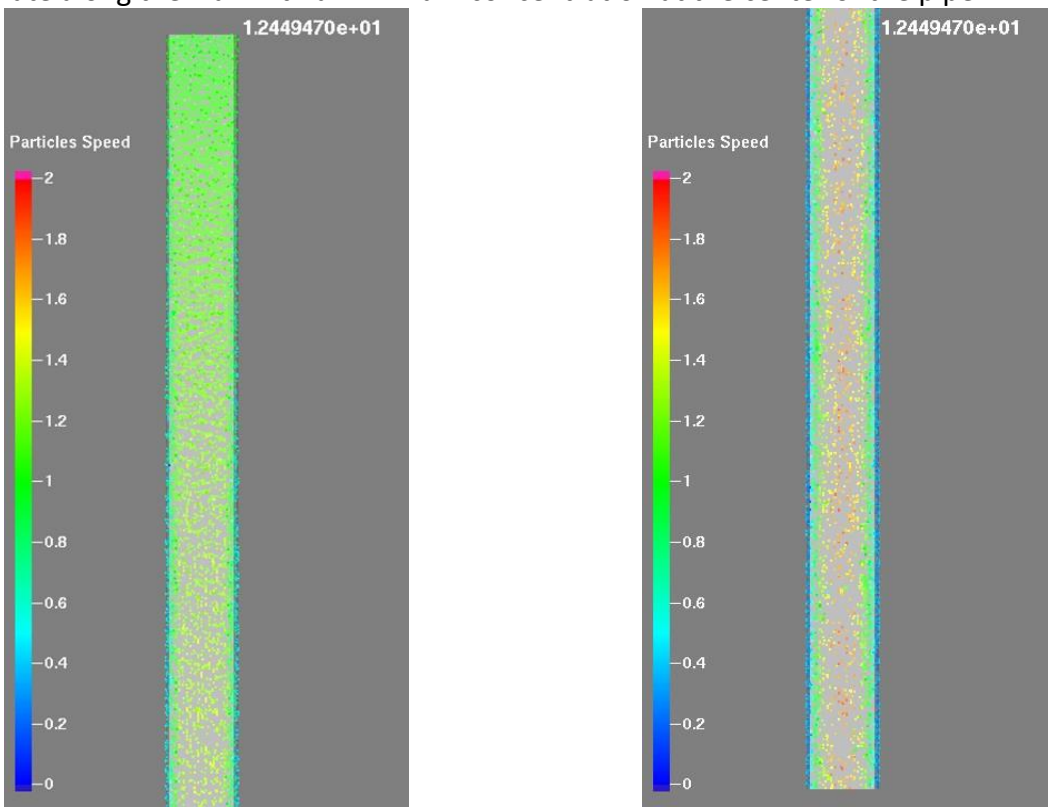

Figure 5-3: Simulation results for dilute slurry (2%) in pipe geometry for a Re 5000. Figures were taken at simulation time of 12.4 sec. Computational particles are color coded by velocity magnitude. (Left) Close up of top of geometry where particles are introduced uniformly. (Right) Close up of bottom of geometry, flow exit.

The simulation results for dilute slurry were consistent with the theoretical, single-phase flow development, and showed that a length of about 50 * L/D was sufficient to fully develop the flow. Simulations of volume fraction of 10% on the other hand, showed that at larger Φ, the particles disrupt the velocity of the liquid phase, creating more turbulence and in fact, aiding in an early onset of fully developed turbulence.
Simulations at higher Φ with varying pipe lengths were attempted, but these geometry/slurry combinations were unstable and the model was not able to run. For this reason we utilized the small geometry tank to further the analysis of flow development in the pipe just before the exit.

5.3.2 Small Tank

Three simulations with varying length pipe feeding into the small tank were run. The geometries are shown in Figure 5-4. As noted from the earlier simulations, shorter pipes seem to result in a delayed development of the jet turbulence. The hypothesis was that the flow entering the tank was not fully turbulent and that a longer pipe would allow the development of turbulence before the jet is created. This was consistent with the results we found.

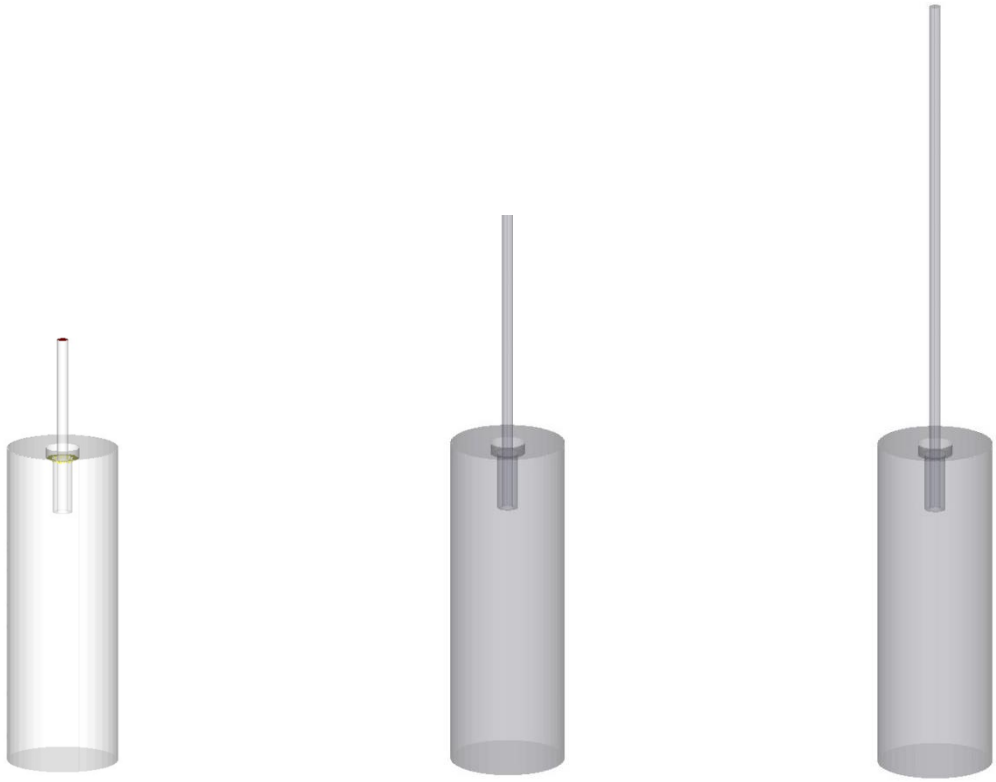

L/D =10 **L/D =25** **L/D =50**

Figure 5-4: Illustration of the geometries used to study the effect of entrance length into the small tank.

Both fluid velocity and particle locations were used to assess the pipe length required for proper flow development. A comparison of the liquid phase downward velocity revealed that in fact, with shorter pipe, the velocity profile at the jet entrance is not fully developed. This is illustrated in Figure 5-5, where a cross section of the geometry is shown for all three

simulations. The downward fluid velocity is color coded by magnitude and it shows that for the L/D = 10 simulation, little to no turbulence in the pipe is present. On the contrary, the downward fluid velocity approaches zero at the wall (as expected) but is shown to be highly turbulent in the rest of the pipe prior to entering the tank. According to the velocity profiles we concluded that for dense slurry a L/D of 25 was sufficient to fully developed turbulence prior to injection. The analysis of the particle distribution around the nozzle revealed that no delay in the onset of turbulent behavior of the jet was found for L/D =25 or 50 see Figure 5-6. This supports our conclusion that in fact the delay was due to the underdevelopment of the fluid velocity profile in the injection pipe.

L/D =10 **L/D =25** **L/D =50**

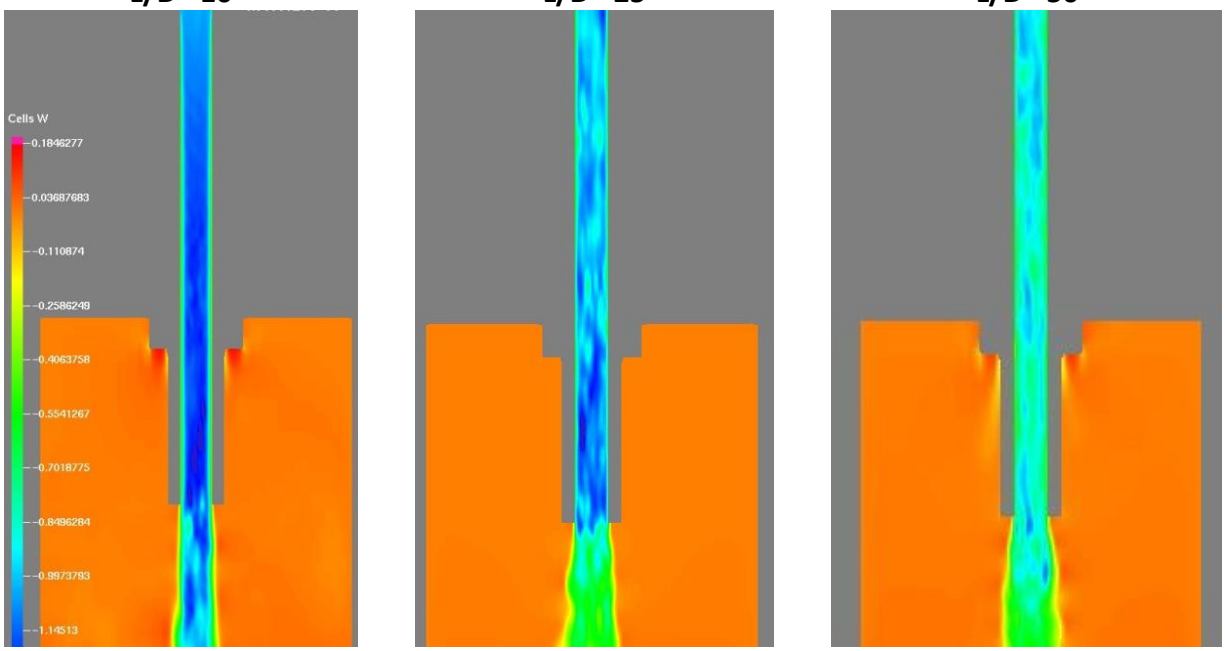

Figure 5-5: Comparison of the magnitude of downward velocity at the nozzle for the three simulations with varying entry length pipe. Figures are taken at the tank cross section.

L/D =10 **L/D =25** **L/D =50**

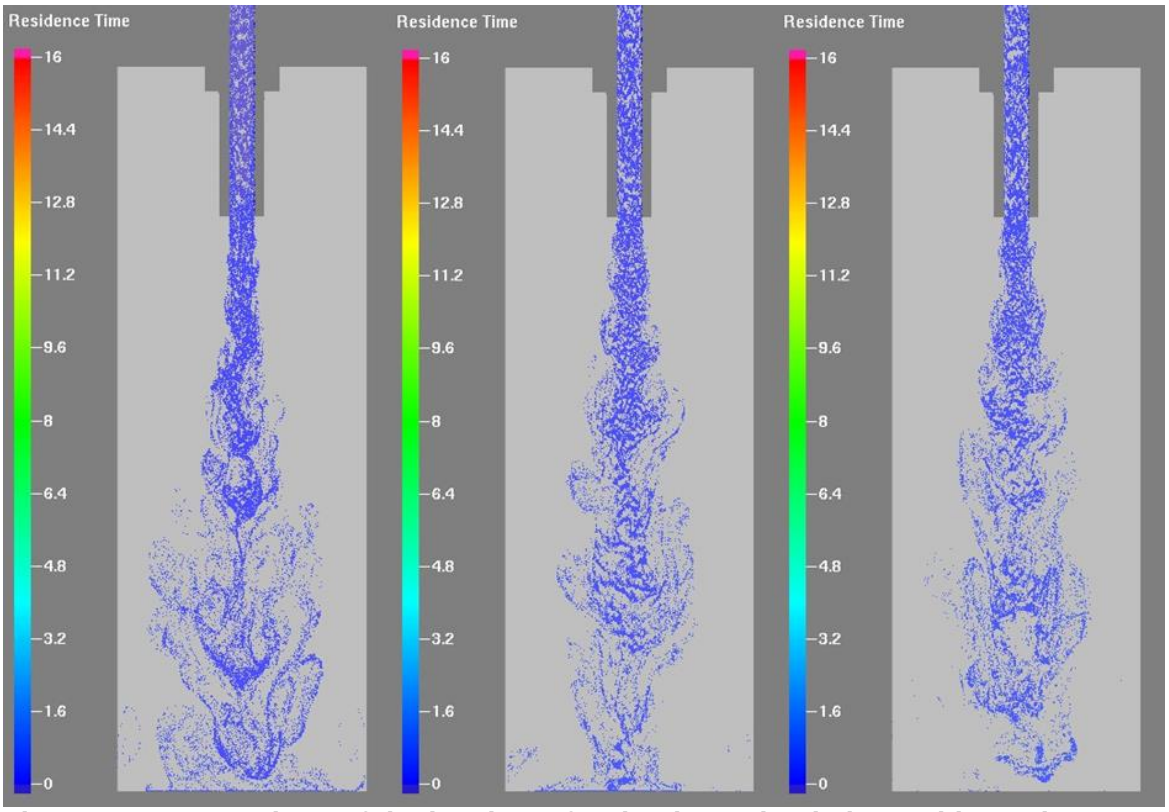

Figure 5-6: Comparison of the jet shape for the three simulations with varying entry length pipe. Particles are shown to illustrate the onset of jet turbulence

5.4 Flow velocity and Volume fraction dependence

A set of simulations with varying flow velocity and larger particles concentration was run to test the limit of the computational model, simulations parameters are included in Table 5-1 for reference. For these simulations an entrance length pipe of L/D of 25 was used. As the Re is increased, it is found that even though the simulations are still stable, they do require a much longer time to run (included in Table 5-1). This is particularly evident as the volume fraction of the particles is increased to 25%. Nonetheless, we found that despite the higher velocities, no difference in the pipe turbulence development is found. An illustration comparing the jet shape as a function of the Re is shown in Figure 5-7. A more rigorous analysis will be conducted in the large tank, where the wall effects won't be predominant as in this geometry.

Table 5-1: Small tank set of simulations parameters and time requirement.

Simulation Code	ϕ	Re	Time to run [days]
ST 1	0	14000	1
ST 2	2	14000	18
ST 3	15	3000	7
ST 4	15	7000	12
ST 5	15	10000	14
ST 6	25	7000	21

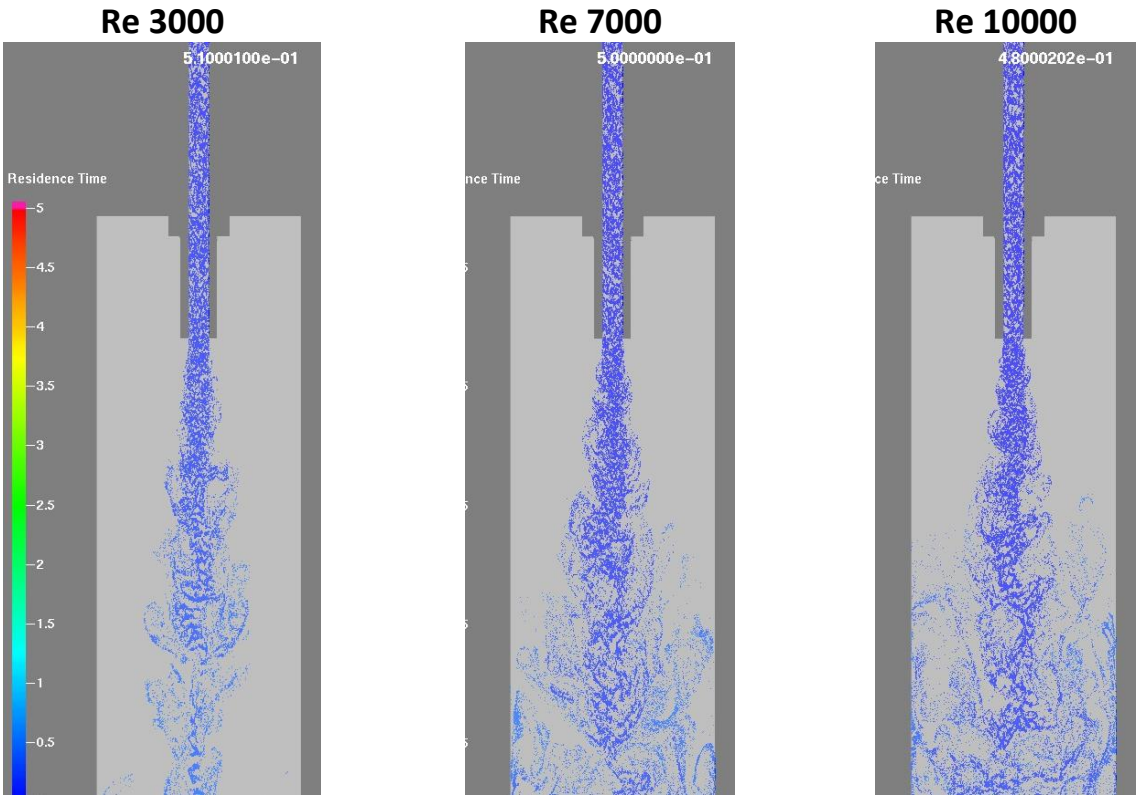

Figure 5-7: Schematic of jet flow in small tank geometry for varying Re.

This page intentionally left blank

6 SLURRY JETS RESULTS: PHASE 2

The second phase of this project is concerned with the characterization of slurry jets as a function of the main controlling parameters. All the simulations ran for this purpose used the large tank geometry as introduced in Figure 3-4 (right) with an entrance pipe length of at least L/D= 25. For reference a list of the variable labels is given in Table 6-1, to note that particle velocities and fluid velocity have distinct notations.

Water-phase variables		Solid-phase variables	
W	Water phase downward velocity (z direction)	**Velz**	Particles downward velocity (z direction)
W_C	Centerline downward velocity (z direction)	**$Velz_0$**	Particles centerline downward velocity (z direction)
b_w	Jet width based on jet water phase velocity	**b_s**	Jet width based on particle concentration phase velocity
		Φ	Particles volume fraction

Table 6-1: List of variable labels used for data processing.

6.1 Flow Rate Dependence

The study of flow rate dependence on jet development and particle distribution was carried out by varying the jet Re from 3000 to 10000. For simplicity these simulations were run for slurries that all have identical volume fraction Φ=15% and are listed below.

Simulation Code	ϕ	Re	Particle size [μm]	L/D
LT 6	15	3000	90-150	25
LT 5	15	7000	90-150	25
LT 7	15	10000	90-150	25

Subset of Table 3-3.

6.1.1 Fluid Velocity Distribution

The velocity profiles of the jets were found to be self-similar and follow Gaussian distribution. An example of the typical shape of velocity profile is given in Figure 6-1 for a series of depths (distance from the nozzle). The magnitude of the fluid phase centerline velocity (at r=0) was evaluated as a function of depth and it was used to characterize and compare the different simulations. In all cases it was found that the centerline velocity rapidly decrease with depth until a plateau is reached at about z/D = 60. This is illustrated in Figure 6-2, where the centerline water velocity is compared for three simulations with Re 3000, 7000 and 10000. Despite the initial larger velocity of the jets (with high Re), all simulations show a plateau velocity of around 0.3 m/s.

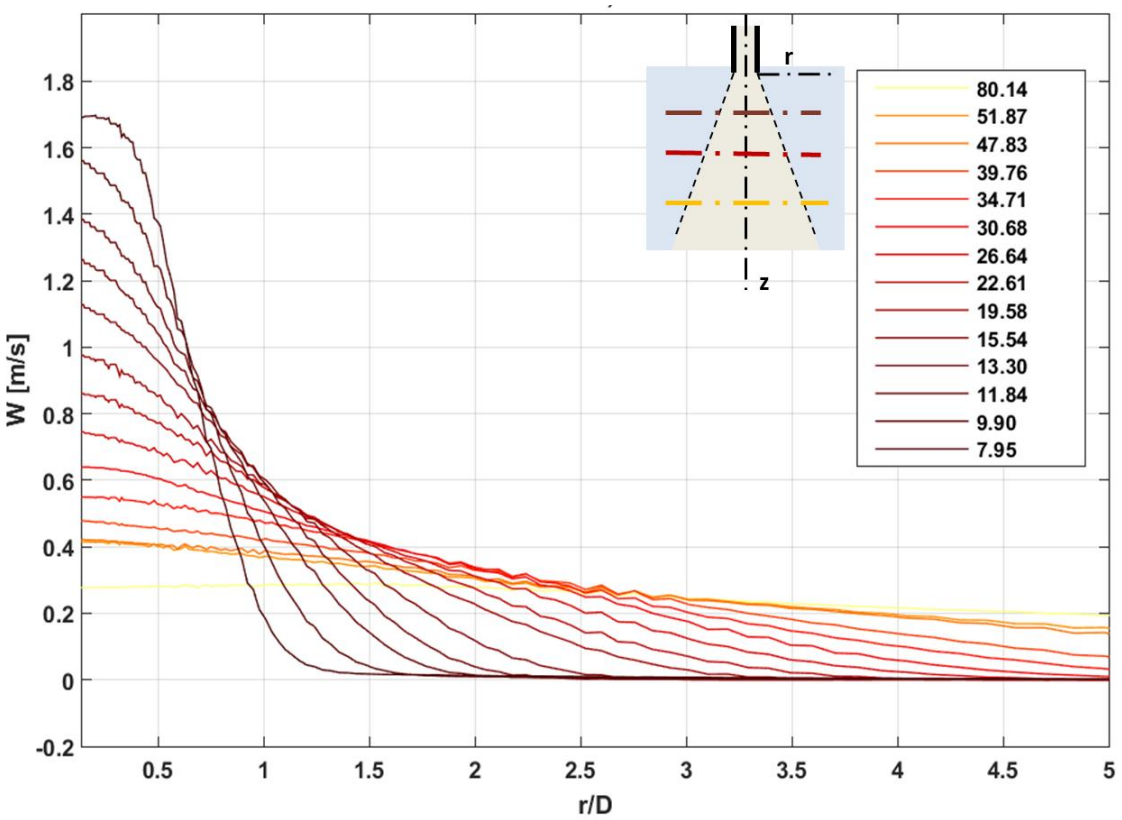

Figure 6-1: Fluid-phase downward velocity profile of simulation with Re 10000 as a function of radial distance for a series of depths. Depths are color coded by vertical distance, z/D.

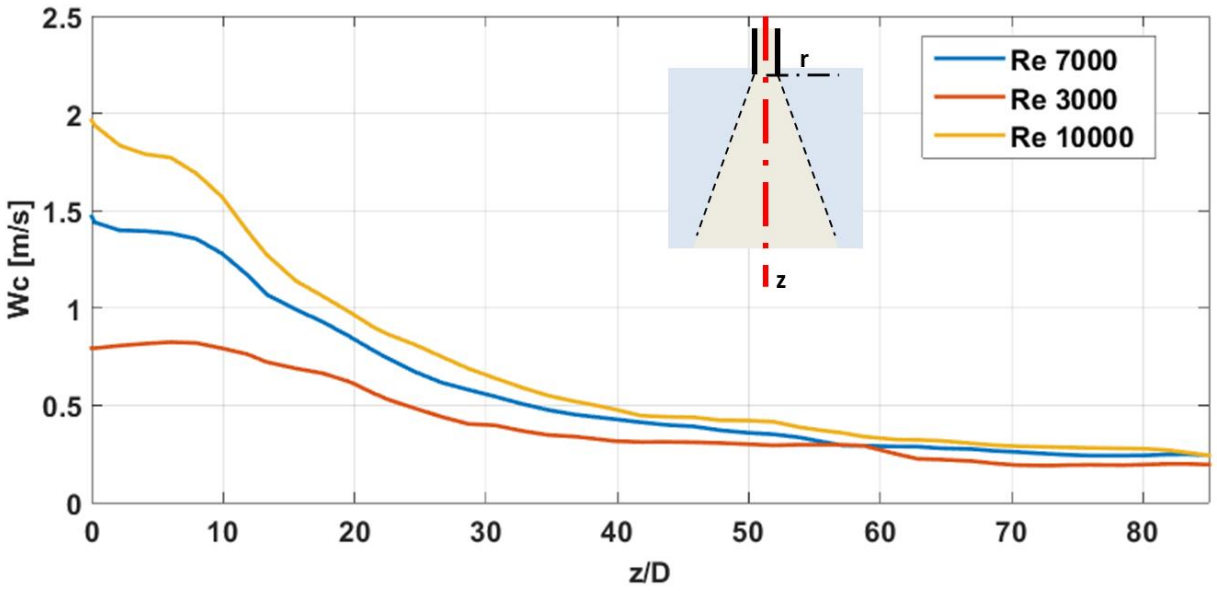

Figure 6-2: Water phase centerline velocity (W_C) as a function of three different Re. The volume fraction for the simulations was kept constant at Φ=15 %.

As it is shown in Figure 6-2 the centerline velocity does not follow the linear relation as described for single–phase jets, suggesting that in fact, the presence of particles introduce non-linear behavior. The magnitude of the plateau, as we'll see later in the report, is not a function of the slurry volume fraction but it does represent the terminal velocity created by the presence of the particles. The width of the jet water phase b_w, as defined in section 3.2.2.3, was found to increase with the Re and it is shown in Figure 6-3.

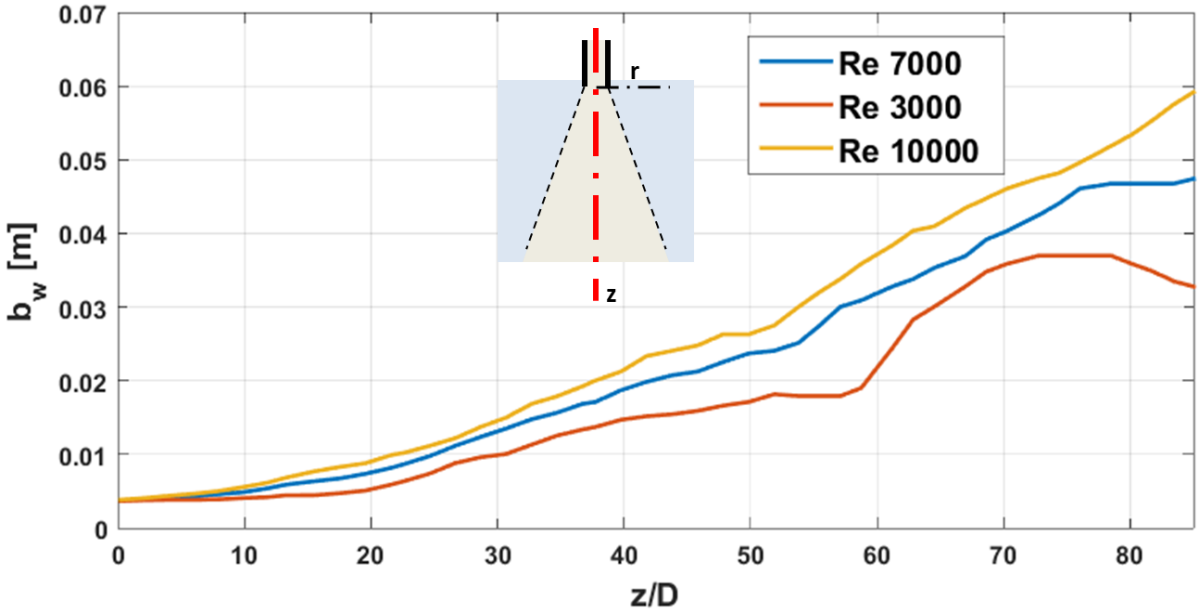

Figure 6-3: Water phase jet width (b_w) as a function of depth (z/D) for three different Re flows.

6.1.2 Solid Velocity Distribution

Similar to what was found for the fluid velocity distribution, we can evaluate particle distribution profile and velocity as a function of Re. The shape of the particle velocity profile is similar to the fluid phase, and it also follows Gaussian distributions. The particles velocity at the jet centerline was evaluated and it is shown in Figure 6-4. As expected the particles for the higher Re simulations start up with higher velocity at the nozzle but, as was shown for the fluid-phase velocity, they reach a plateau at around z/D = 60. The magnitude of this 'particle terminal velocity' is the same as the fluid phase one, indicating that the particles and fluid are moving downward with the same terminal speed.

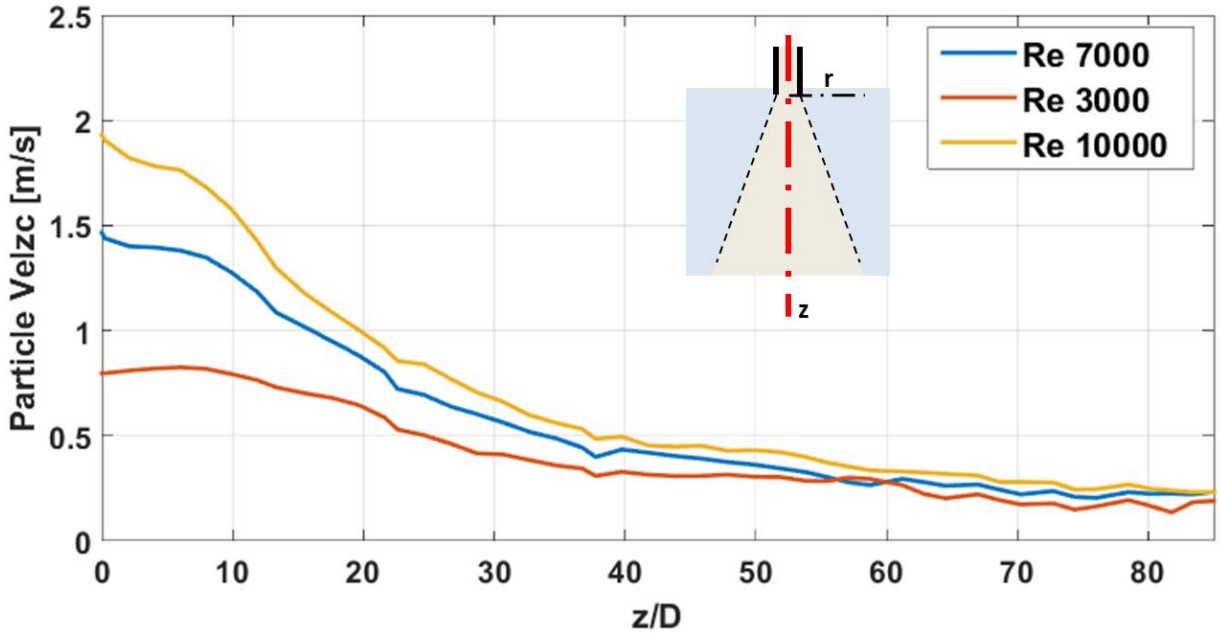

Figure 6-4: Particle centerline velocity ($Velz_C$) as a function of three different Re. The volume fraction for the simulations was kept constant at Φ=15 %.

6.1.3 Concentration Distributions

Particle distribution and concentrations were analyzed by studying both the volume fraction concentration profiles as a function of radial distance (see Figure 6-5) as well as the jet centerline volume fraction as a function of depth. Concentration profiles are found to be similar in shape to velocity profiles introduced in the previous section and no Re dependence was found.

The width of the particle phase of the jet is calculated based on the volume fraction distribution as described in section 3.2.2.3, and is shown in Figure 6-6. A very small dependence on the Re is found. Due to the method used to average particle locations, the solid phase width functions are much noisier than the fluid-phase.

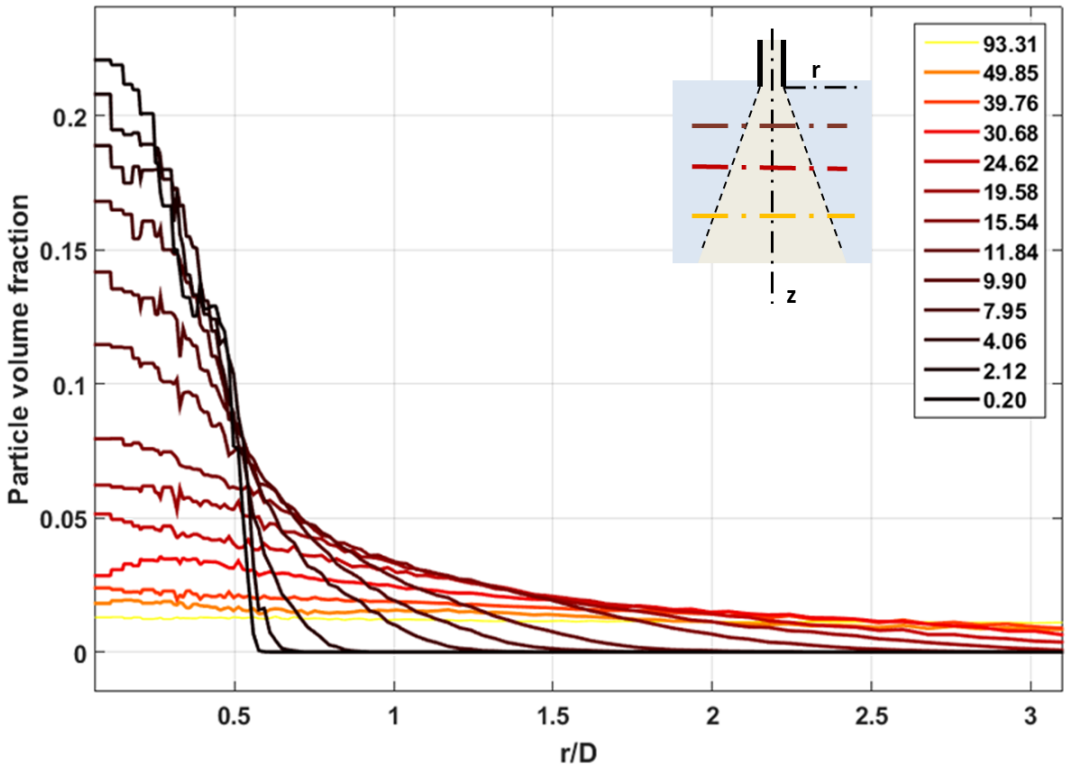

Figure 6-5: Volume fraction distribution profile of simulation with Re # 10000 as a function of radial distance for a series of depths. Depth are color coded by vertical distance, z/D.

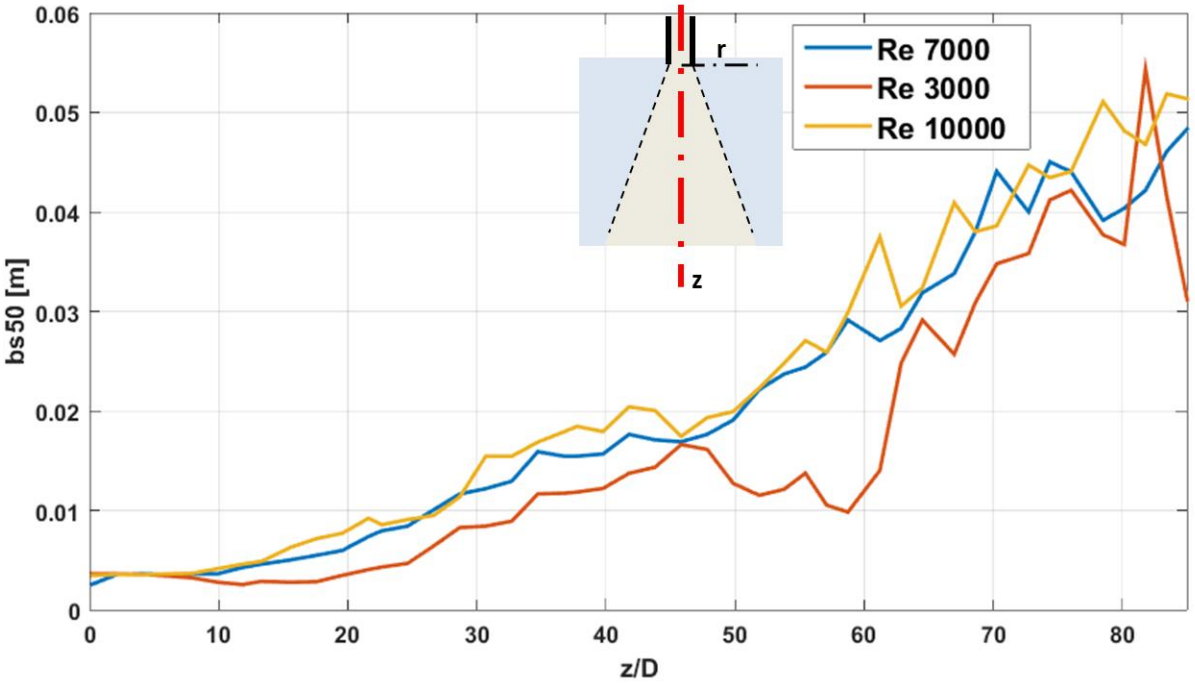

Figure 6-6: Jet width based on particle concentrations as a function of depth for 3 different Re flows.

6.1.4 Jet Spreading

Jet spreading of a two-phase jet can be characterized by comparing the fluid phase width to the particle based width. We define λ as:

$$\lambda = \frac{b_w}{b_{s1/2}} \qquad \textbf{(6-1)}$$

A spreading rate of 1 is indicative of a jet that spreads at the same rate as its water phase, while a spreading rate smaller than 1 indicates that the particle phase doesn't spread as far as its water phase. Figure 6-7 illustrated the spreading rate for all three slurries. Noise in the data makes it difficult to differentiate between varying Re but in all cases λ is found to be smaller than 1 and shows that loaded slurry does nor spread as much as water.

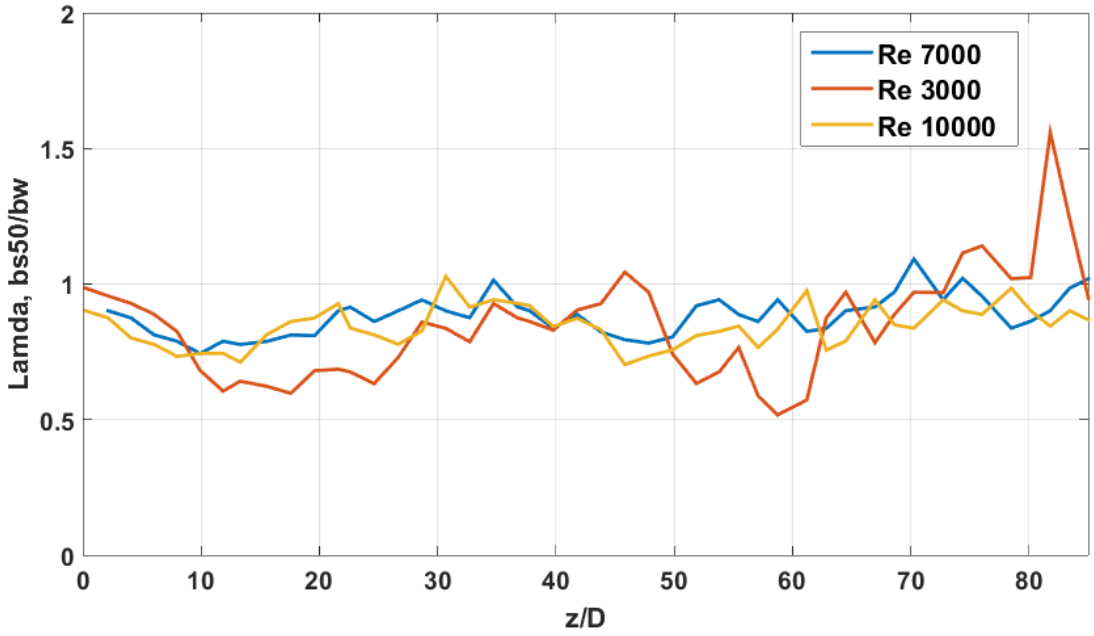

Figure 6-7: Jet spreading parameter λ , for different Re flows.

6.2 Volume Fraction Dependence

The particle concentration dependence for slurry jets was studied. Simulations for solutions with volume fraction that varied from 1 to 25% were run at a Reynold number of 10000.

Sim. Code	ϕ	Re	Particle size [μm]	L/D
LT 8	1	10000	90-150	25
LT 7	15	10000	90-150	25
LT 10	25	10000	90-150	25

Subset of Table 3-3.

6.2.1 *Fluid Velocity Distribution*

The centerline velocity distribution for the three different simulations at varying volume fraction Φ was compared to study the effect of particles on the jet development. A plot of the non-dimensionalized centerline velocity for the fluid phase is shown in Figure 6-8 (top). It is interesting to note that the case of very dilute solution (Φ =1% simulation) is characterized by an initial sharp decrease in the centerline velocity (much greater than for the dense slurries). This rapid decrease of the centerline velocity also corresponds to a larger spread of the water phase jet width as shown in Figure 6-9. After this steep spreading and fast deceleration of the flow, the downward centerline velocity slows down at a much slower rate as it approached zero.

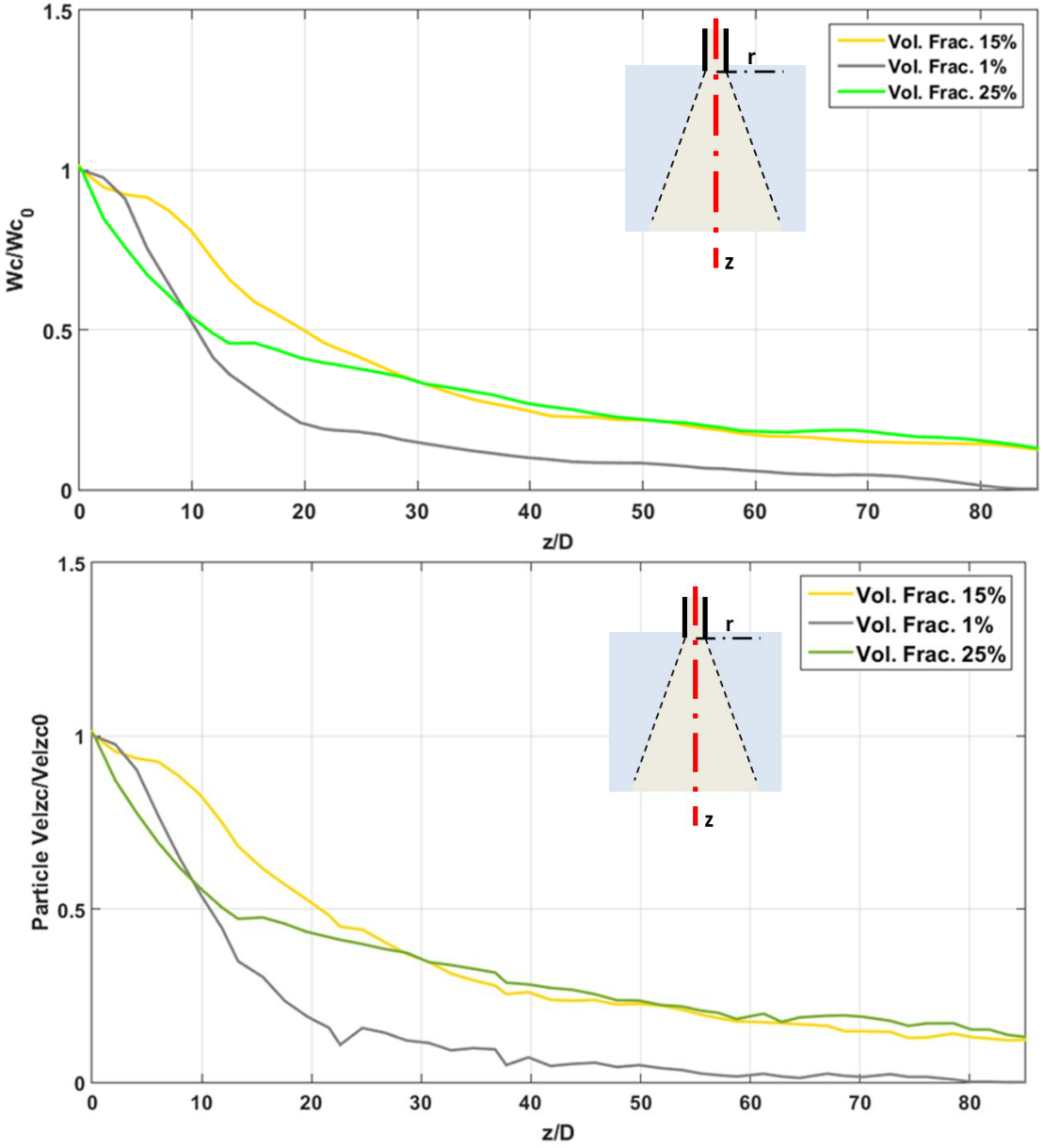

Figure 6-8: (top) Water phase centerline velocity (W_C) non-dimensionalized by W_{C0} (W_C at nozzle) for three different volume fractions. (bottom) Particle centerline velocity ($Velz_C$) non-dimensionalized by $Velz_{C0}$ ($Velz_C$ at jet nozzle) for different volume fractions.

The centerline velocities for the dense slurries, on the other hand, are found to be sensitive to the slurry volume fraction near the nozzle, where the jet turbulence/vortexes are starting to develop. After a distance of about 30 diameters away from the nozzle the non-dimensional velocities reach the same value and a more gradual flow deceleration is found. As opposed to the behavior of the very dilute slurry, the downward velocity of the slurry jets approaches a constant value which is independent of the volume fraction, but it is induced by the presence of particles in solution.

The solid-phase velocity analysis for the three simulations (varying Φ) have found that the particle velocity exhibit a very similar behavior to the water-phase velocity. A plot of the non-dimensionalized particle velocities is given in Figure 6-8 (bottom). The particle centerline at large distance (z/D) is found to approach the same fluid-phase velocity and confirmed that the particle and fluid are moving downward with the same terminal speed.

A comparison of the jets width, based on the water-phase velocity, is shown in Figure 6-9. The width of the dilute jet is significantly larger than the dense slurry jets which instead are found to decrease with volume fraction. This suggests that the presence of particles hinder the radial spreading of the jet, while increasing the downward speed resulting in a tighter, faster jet. This effect increases as more particles (larger Φ) are introduced. This phenomenon is also confirmed by the results shown in Figure 6-10, where λ is plotted for all 3 volume fraction slurries. As expected the spreading rate for the dilute solution is around 1, while it decreases significantly as the volume fracture of the slurry is increased.

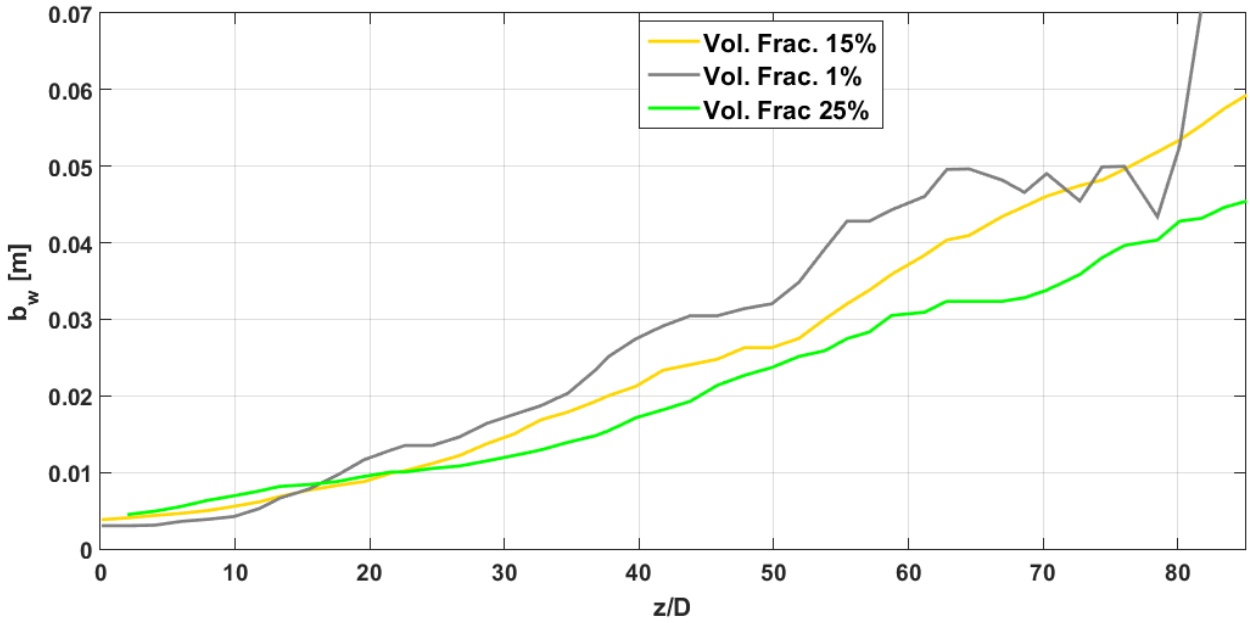

Figure 6-9 Water phase jet width as a function of depth for different volume fraction slurries.

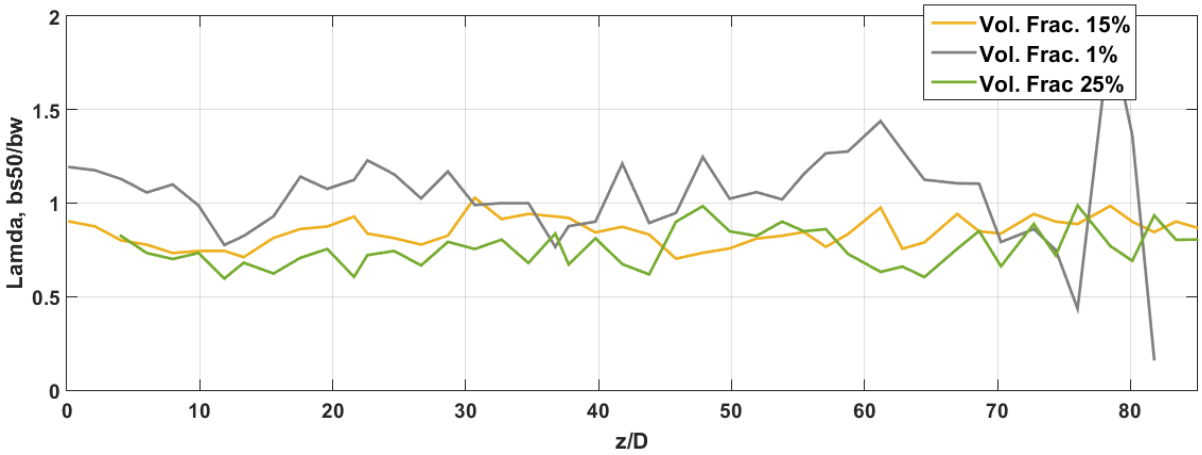

Figure 6-10: Jet spreading parameter λ , for varying volume fractions.

6.3 Particle Size and Distribution Dependence

Sim. Code	ϕ	Re	Particle size [μm]	L/D
LT 11	15	10000	5	25
LT 12	15	10000	15	25
LT 13	15	10000	150	25
LT 7	15	10000	90-150	25
LT 14	15	10000	1-5	25
LT 15	15	10000	50-100	25
LT 16	15	10000	5-100	25

Subset of Table 3-3.

6.3.1 Particle Size Study

A plan to study the jet development as a function of particle size and distribution was made. Difficulties with the interpretation of the simulation results are found when slurries with relatively small particles were introduced. A set of simulations were run with slurries at Φ of 15% and monodisperse particles that varied from 5 μm to 150 μm. Illustrations of the types of jet resulting from these tests are shown in Figure 6-11. As shown figure, small particles slurry did not developed any turbulence, which is unrealistic at the Re 10000. Some turbulence and jet spreading was found for the 15 μm slurry (Figure 6-11 center), but it still does not match with what one would expect from a slurry flow at high Re.

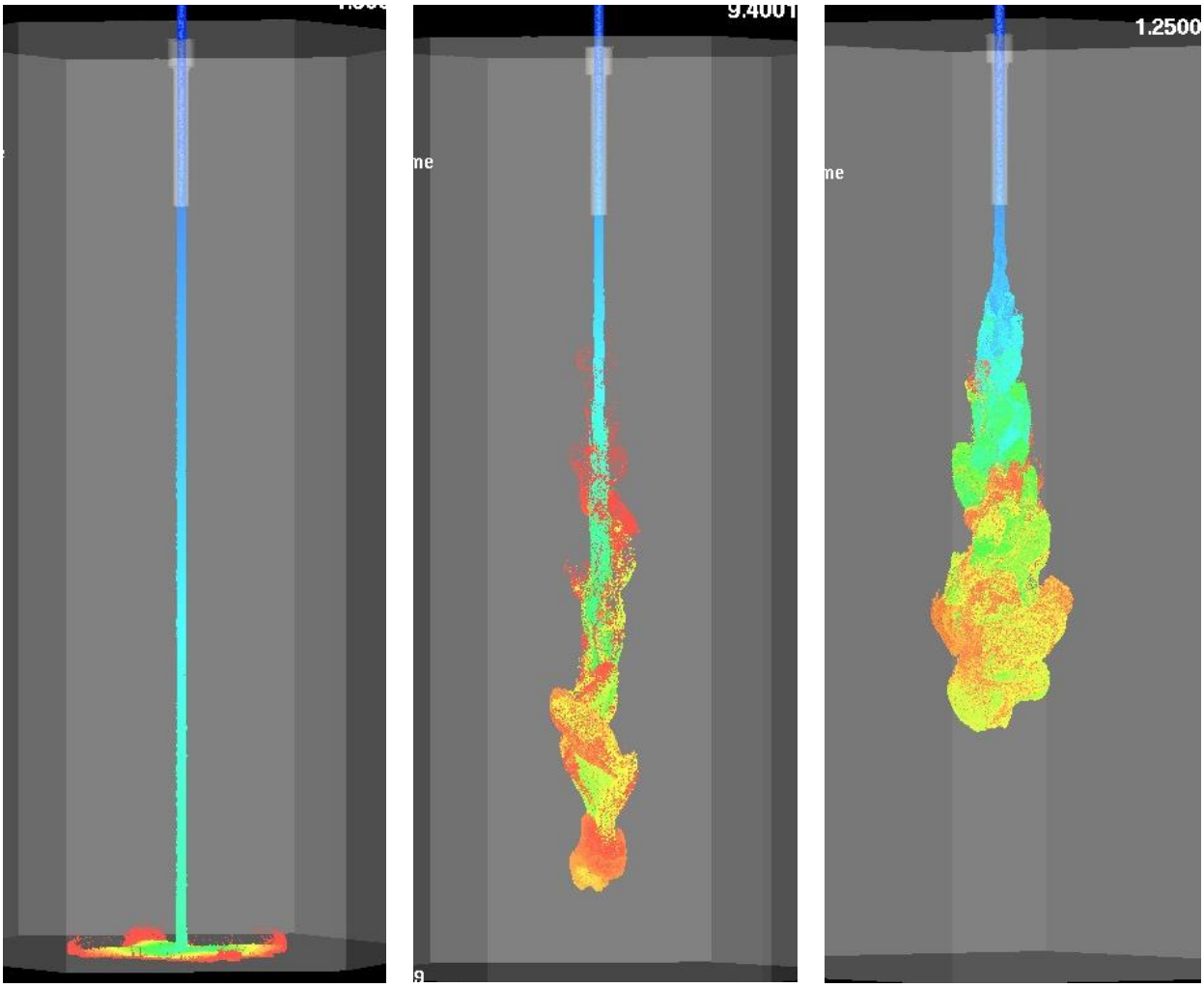

d =5 μm *d* =15 μm *d* =150 μm

Figure 6-11: Illustration of jet shape as a function of particle size.

The lack of jet spreading was more quantitatively studied by evaluating the magnitude of the centerline velocity and the width of jet. As shown in Figure 6-12, the velocity of the smaller particle slurry does not decrease with depth and therefore it does not grow radially (as confirmed in Figure 6-13).

The reason for the unrealistic results with smaller particles (5 μm and possibly 15 μm) is still under investigation. It is suspected that we have reached a limit of the computational model and we hope to understand the limiting factors and benchmark these results against laboratory experiments.

The results obtained for the larger particle simulations (150 μm) are, on the other hand, consistent with experimental results. Furthermore, we found that the monodisperse based slurry behaved identical to the test case, LT 07 (validated with laboratory experiment), with a normal particle size distribution of 90-150 μm. Comparisons of jet centerline velocity and the widths between slurry of 150μm monodisperse particles with LT07 are shown in Figure 6-15 and Figure 6-16.

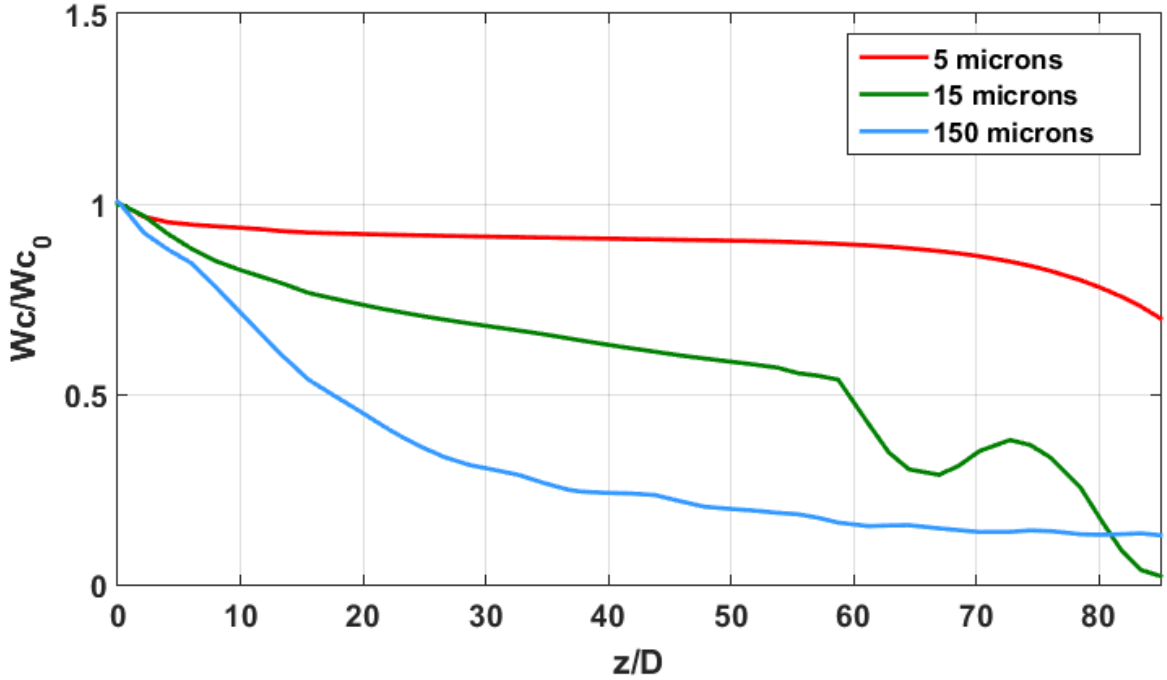

Figure 6-12: Water phase centerline velocity (W_C) non-dimensionalized by W_{C0} (W_C at nozzle) for different particle size slurries.

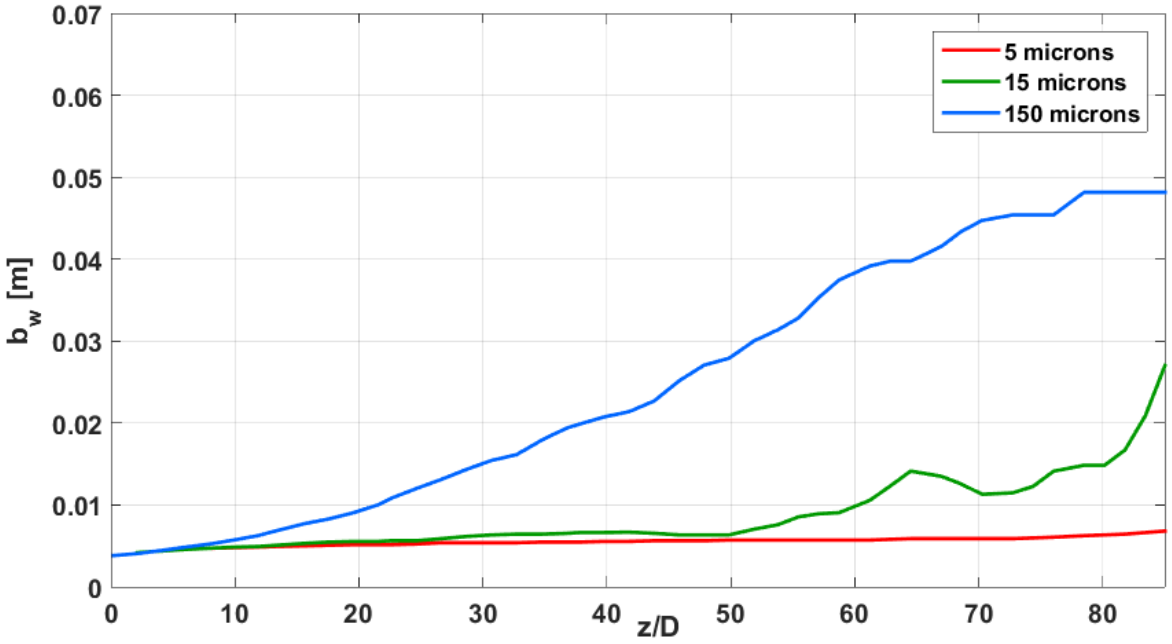

Figure 6-13: Water phase jet width as a function of depth for different particle size slurries.

6.3.2 Particle Size Distribution

A set of simulations that compared slurries with different particle size distributions (PSD) were run. An illustration of the simulations results are given in Figure 6-14. It is unclear at this point if the distribution of the particle size has a measurable effect on the jet development, but the shape of the jets suggest that larger particles (average) results in bigger jet spreading.

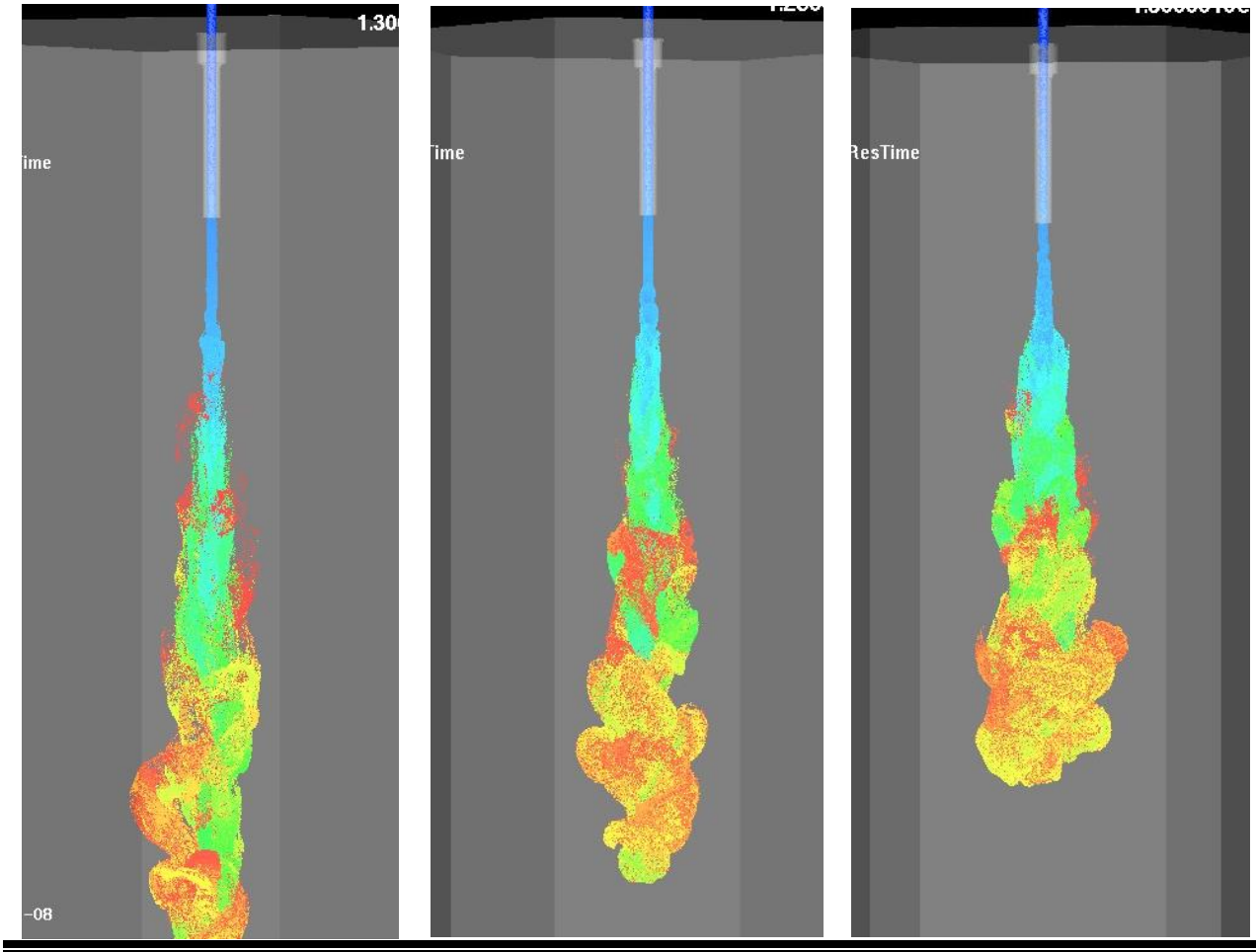

(LT16)	(LT15)	(LT 07)
PSD = 5-100 μm	PSD = 50-100 μm	PSD = 90-150 μm
Average *d* = 50 μm	Average *d* = 75 μm	Average *d* = 120 μm

Figure 6-14: Illustration of jet shape for a set of slurries with varying PSD.

The centerline velocity for the simulations with varying PSD is shown in Figure 6-15. For reference, the results for the monodispere slurry with particles of 150 μm are also shown. As previously noted, very little difference is found in the results between monodisperse 150 μm with LT 07 both in centerline velocity and jet width. This suggests that PSD has very little effect on the jet, but in fact, the average particle size, might yield a stronger dependence.

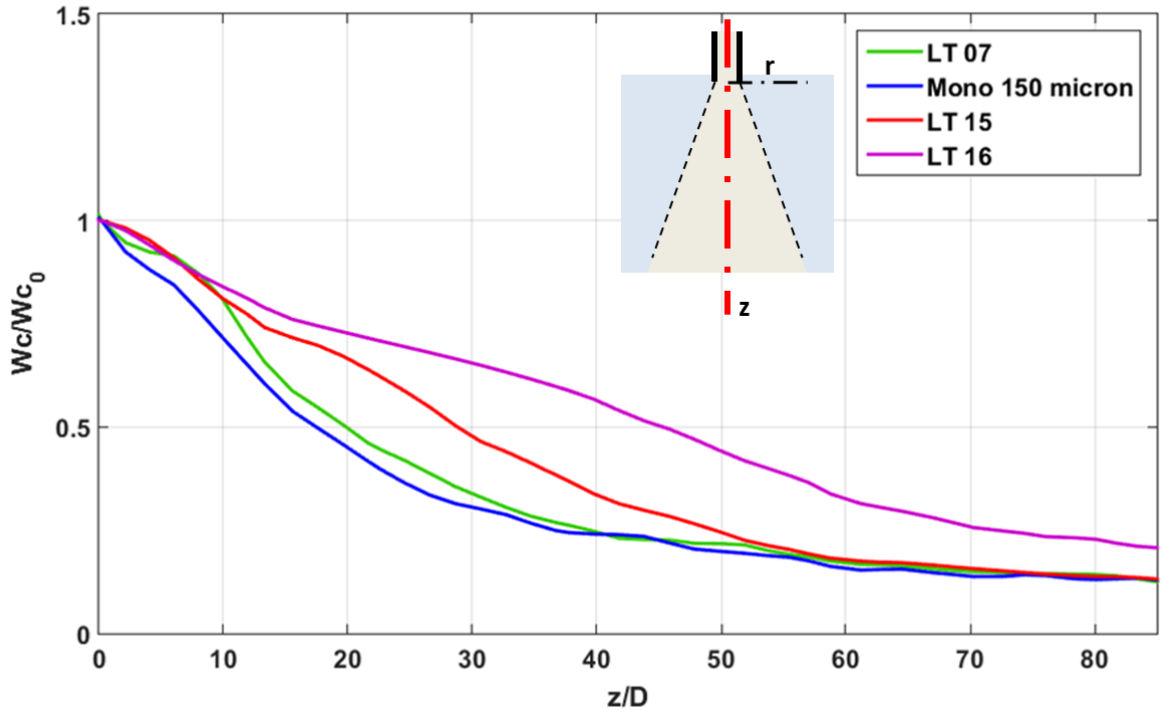

Figure 6-15: Water phase centerline velocity (W_C) non-dimensionalized by W_{C0} (W_C at nozzle) for different particle size slurries.

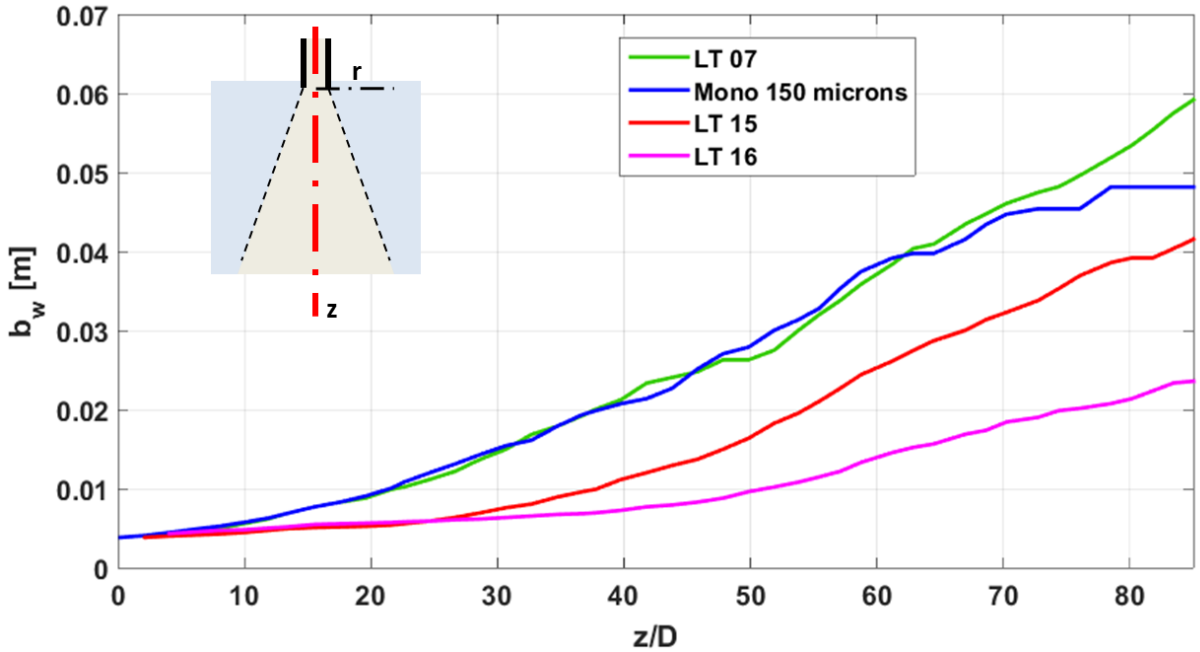

Figure 6-16: Water phase jet width for different particle size slurries.

This page intentionally left blank

7 CONCLUSIONS

This study evaluated the performance of the Barracuda software in modeling high rates and high volume fraction slurry flow. It was found that Barracuda was able to simulate slurry jet flows at Re up to 15000 and it was tested at particles loading up to Φ =25%. Some of the limitations consisted of the long time requirement for simulations to run, which eventually limits its applicability to model flow in cavern size geometries. Another apparent limit of the model which is still under investigation, was found with slurries of very small particle sizes; this resulted in unrealistic flow patterns.

The second phase of this project found that both Re and Φ affect the jet width and its velocity. The spreading rate λ was found to be smaller than 1 for all slurry flows, and it was dependent on the slurry volume fraction. The study also suggested that the particle size distribution does not have a large influence on flow development, at least in the parameter space that was tested. The effect of particle size is still under investigation.

For clarity the results of this study have been added to Table 7-1 which was first introduced in section 2.4.2. This study confirmed some of the results published in the literature and was able to access parameters spaces (higher volume fractions) which were previously unavailable.

Table 7-1 Effect of particle properties on slurry jets of various particle loading as found in the literature (in black) and as found in this study (in red).

		Jet spreading	Jet width	Centerline velocity
		λ	b_w	W_c
Single-phase	$\Phi = 0$		• Linear increase with distance from the nozzle	• Linear decay with distance from the nozzle
Dilute	$0 < \Phi < 1$	• Decrease with Φ • Decrease with larger *d*	• Similar to single phase at small distances, but decrease farther from the nozzle	• Same as single phase
Semi-dilute	$1 < \Phi < 5$	• Decrease with Φ • Insensitive to *d*	• Similar to single phase at small distances, but decrease farther from the nozzle	• Increase with Φ
Dense	$5 < \Phi < 15$	• Decrease with Φ	• Decrease with Φ • Increase with **Re** • Insensitive to **PSD**	• Increase with Φ • Increase with Φ a large distance from the nozzle • Insensitive to **PSD**
Very dense	$\Phi > 15$	• Decrease with Φ	• Decrease with Φ • Increase with Re • Insensitive to **PSD**	• Increase with Φ a large distance from the nozzle • Insensitive to **PSD**

REFERENCES

1. Crotogino, F., C. Behrendt, and J. Hackney, (1997) *Bibliography for Cavern Abandonment*, in *SMRI Project No. 97-0002*, Solution Mining Institute.
2. Bettin, G., (2013) *Letter Report: Cavern Abandonment Literature Review*, Albuquerque, NM. p. 15.
3. Berest, P., et al., (2001) *A Salt Cavern Abandonment Test.* Journal of Rock Mechanics & Mining Sciences, **38**: p. 357-368.
4. Berest P. and Brouard B. *Behavior of Sealed Solution-Mined Caverns*. (1995) *Solution Mining Research Institute Spring Meeting*. New Orleans, LA.
5. Durup, J.G., F. Vidal, and C. Rolin, *Pilot Abandonment Test of a Very Deep Gas Storage Salt Cavern.* Oil & Gas Science and Technology - Revue de l'IFP, 2007. **62**(3): p. 287-296.
6. Brennen., C.E., *Granular Flows -Chap. 13*, in *Fundamentals of Multiphase Flow* 2005, Cambridge University Press.
7. Wilson, K.C., G.R. Addie, and A. Sellgren, (2006) *Slurry Transport Using Centrifugal Pumps*: Springer Science+Business Media, Inc.
8. Clayton, T., (2006) *Multiphase Flow Handbook,* Boca Raton, FL: CRC Press.
9. Doron, P. and D. Barnea, (1996) *Flow Pattern Maps for Solid-Liquid Flow in Pipes.* International Journal of Multiphase Flow, **22**(2): p. 273-283.
10. Ball, C.G., H. Fellouah, and A. Pollard, (2012) *The Flow Field in Turbulent Round Free Jets.* Progress in Aerospace Science, **50**: p. 1-26.
11. Elghobashi, S., (1994) *On Predicting Particle-Laden Turbulent Flows.* Applied Scientific Research, **52**: p. 309-329.
12. Brush, L.M., (1962) *Exploratory Study of Sediment Diffusion.* Journal of Geophysical Research, **67**(4): p. 1427-1433.
13. Virdung, T. and A. Rasmunson, (2007) *Hydrodynamic Properties of a Turbulent Confined Solid-Liquid Jet Evaluated Using PIV and CFD.* Chemical Engineering Science. **62**: p. 5963-5978.
14. Jiang, J., A. Law, and N. Cheng, (2005) *Two-Phase Analysis of Vertical Sediment-Laden Jets.* Journal of Engineering Mechanics. **131**(3): p. 308-318.
15. Parthasarathy, R.N. and G.M. Faeth, (1987) *Structure of Particle-laden Turbulent Water Jets in Still Water.* International Journal of Multiphase Flow. **13**(5): p. 699-716.
16. Hall, N., et al., (2010) *Experimental Study of Sand and Slurry Jets in Water* Journal of Hydraulic Engineering. **136**(10): p. 727-738.
17. Azimi, A., D.Z. Zhu, and N. Rajaratnam, (2012) *Computational Investigation of Vertical Slurry Jets in Water.* International Journal of Multiphase Flow. **47**: p. 94-114.
18. Snider, D.M., P.J. O'Rourke, and M.J. Andrews, (1998) *Sediment Flow in Inclined Vessels Calculated Using a Multiphase Particle-in-Cell Model for Dense Particle Flows.* International Journal of Multiphase Flow. **24**: p. 1359-1382.
19. Snider, D.M., (2007) *Three Fundamental Granular Flow Experiments and CPFD Predictions.* Power Technology. **176**: p. 36-46.
20. Metzner, A.B., (1985) *Rheology of suspensions in polymeric liquids.* Journal of Rheology. **29**(6).

DISTRIBUTION

1	MS0899	Technical Library	9536 (electronic copy)
1	MS0359	D. Chavez, LDRD Office	1911


Sandia National Laboratories